

# THE H<sub>I</sub> GAS IN BLUE COMPACT DWARF GALAXIES

François Levrier

Professor Trinh X. Thuan,  
Astronomy Department, University of Virginia,  
530 Mc Cormick Road,  
Charlottesville, VA 22903  
txt@virginia.edu

Doctor John E. Hibbard,  
National Radio Astronomy Observatory,  
520 Edgemont Road,  
Charlottesville, VA 22903-2475  
jhibbard@nrao.edu

Stage de recherche, MIP 2e année  
Janvier-Juin 1998

# Abstract

The neutral atomic hydrogen (HI) in four blue compact dwarf galaxies (BCDs), NGC 2366, I Zw 49, VII Zw 403 and Haro 2, was observed with the Very Large Array (VLA) between 1984 and 1992.

BCDs are dwarf galaxies currently undergoing bursts of intense star formation. There have not yet been many studies of the HI content and dynamics in these objects through interferometric data, even though neutral hydrogen is the original element from which stars eventually form.

We find evidence of a disturbed medium, with “clumps” and “holes”, and the HI does not seem to lie in a regular, rotating disk, although we obtain good, stable results when kinematically modeling two of our galaxies (NGC 2366 and I Zw 49) as disklike distributions. For VII Zw 403 and Haro 2, random motions seem to be as or more important than rotational motions. We detect HI cloud companions for I Zw 49 and Haro 2, which may be yet another evidence of a disturbed medium. We finally address the problem of dark matter, presenting a comparison between our sample and another studied by Lo, Sargent and Young [26] consisting of nine dwarf irregulars (dIs). We conclude that the two types of dwarfs are very similar, save for their star formation activity, which results in a greater velocity dispersion in BCDs than in dIs.

# Résumé

Nous présentons des observations, faites avec le Very Large Array (VLA) entre 1984 et 1992, du contenu en hydrogène atomique neutre (HI) de quatre galaxies bleues compactes (BCDs), à savoir NGC 2366, I Zw 49, VII Zw 403 et Haro 2.

Les galaxies bleues compactes sont des naines en phase d'intense formation d'étoiles. Les études interférométriques de la distribution et de la dynamique du gaz que ces objets contiennent sont encore peu nombreuses, alors même que c'est à partir de cet élément primordial, l'hydrogène neutre, que se forment finalement les étoiles.

Nous observons un milieu très perturbé, avec de nombreux “trous” et “agrégats”, et où la distribution du gaz ne semble pas évoquer un disque en rotation, bien que les modélisations cinématiques de deux de nos objets (NGC 2366 et I Zw 49) suggèrent de telles configurations. En ce qui concerne VII Zw 403 et Haro 2, il semble que les mouvements chaotiques soient au moins aussi importants, sinon plus, que la rotation. Nous détectons la présence de nuages compagnons pour deux de nos galaxies, I Zw 49 et Haro 2, ce qui pourrait également montrer que nous avons affaire à des milieux perturbés. Finalement, nous nous penchons sur le problème de la masse manquante en présentant une comparaison de notre échantillon avec celui étudié par Lo, Sargent et Young [26], lequel comprenait neuf naines irrégulières (dIs). Nous en concluons que ces deux types de naines sont très semblables, et qu'ils se différencient par leurs taux de formation d'étoiles, plus élevé chez les galaxies bleues compactes, avec pour conséquence que la dispersion des vitesses y est plus grande que dans les naines irrégulières.

# Acknowledgements

I would like to thank Trinh Xuan Thuan, for offering me this unique opportunity to gain an insider's view on the “American Way of Science” and John Hibbard, for all the invaluable help he provided all along this work, from my first steps in *AIPS* to the final draft of my report.

I would also like to thank everyone at NRAO and UVa, faculty, graduate students and staff.

# Contents

<b>1</b>	<b>The objects and the means</b>	<b>5</b>
1.1	Blue Compact Dwarfs (BCDs) . . . . .	5
1.1.1	Introduction . . . . .	5
1.1.2	Metal deficiency . . . . .	5
1.1.3	Starburst galaxies . . . . .	5
1.1.4	Rotational versus chaotic motions . . . . .	6
1.1.5	Our sample . . . . .	6
1.2	Physical principles of interferometry . . . . .	8
1.2.1	Propagation of information . . . . .	8
1.2.2	The spatial coherence function . . . . .	8
1.2.3	Synthesis imaging through Fourier transforms . . . . .	9
1.2.4	The problem of deconvolution . . . . .	9
1.3	Spectral line imaging . . . . .	12
1.3.1	Definition of a spectral line . . . . .	12
1.3.2	The neutral hydrogen line . . . . .	12
1.3.3	The Doppler effect . . . . .	12
1.3.4	Cubes and moments . . . . .	12
1.4	The Very Large Array . . . . .	13
<b>2</b>	<b>The analysis and the results</b>	<b>14</b>
2.1	Data Reduction using the <i>AIPS</i> package . . . . .	14
2.1.1	Introduction . . . . .	14
2.1.2	Editing and Calibration . . . . .	14
2.1.3	Imaging . . . . .	15
2.2	NGC 2366 . . . . .	16
2.2.1	Morphology . . . . .	16
2.2.2	HI flux - comparison with single dish . . . . .	16
2.2.3	Kinematical modeling . . . . .	19
2.2.4	Velocity dispersion . . . . .	20
2.3	I Zw 49 . . . . .	20
2.3.1	Morphology . . . . .	20
2.3.2	HI flux - comparison with single dish . . . . .	20
2.3.3	Kinematical modeling . . . . .	23
2.3.4	Velocity dispersion . . . . .	23
2.4	VII Zw 403 . . . . .	24
2.4.1	Morphology . . . . .	24
2.4.2	HI flux - comparison with single dish . . . . .	24
2.4.3	Kinematical modeling . . . . .	24
2.4.4	Velocity dispersion . . . . .	27

2.5	Haro 2 . . . . .	27
2.5.1	Morphology . . . . .	27
2.5.2	HI flux - comparison with single dish . . . . .	28
2.5.3	Kinematical modeling . . . . .	28
2.5.4	Velocity dispersion . . . . .	28
2.6	The dark matter problem . . . . .	31
2.6.1	A very brief overview . . . . .	31
2.6.2	Dark matter in our sample . . . . .	31

# Chapter 1

## The objects and the means

### 1.1 Blue Compact Dwarfs (BCDs)

#### 1.1.1 Introduction

At the faintest end of the Hubble sequence, the so-called “dwarf” galaxies, with absolute blue magnitudes  $M_B$  typically larger than -18 (let us remember that the greater the magnitude, the fainter the object), have received relatively little attention. Compared to the simple designs of spirals and ellipticals, these systems are quite heterogeneous, with amorphous morphologies. Blue compact dwarfs (BCDs) are a subset of the dwarf class (which includes dwarf ellipticals, dwarf spheroidals and dwarf irregulars) that are defined by the presence of a compact blue component, usually a star-forming cluster. The once overlooked dwarf galaxies have recently taken the center-stage, for, in the theory of *hierarchical clustering* [14], these objects are thought to be the building blocks of larger systems. As a result, they may hold the key to the puzzle of galaxy formation. Dwarf galaxies have a number of interesting properties, which Thuan [47] reviewed at the “Massive Stars in Starbursts” meeting in Baltimore, in 1990. I will now summarize these properties.

#### 1.1.2 Metal deficiency

Since the identification of these objects by Sargent and Searle [37], it has been recognized that BCDs are extremely deficient in heavy elements. As a matter of fact, I Zw 18, one of the very first BCDs discovered, still holds the record of the most metal-poor galaxy known [34, 38], with a metallicity of about a fiftieth of that in the solar neighborhood ( $Z \simeq Z_\odot/50$ ). Even excluding this somewhat extreme case, the metallicity in dwarf galaxies lies typically below  $Z_\odot/3$  [28].

#### 1.1.3 Starburst galaxies

Such metal deficiency requires that these objects have undergone little chemical evolution throughout their history<sup>1</sup>. Their present-day star formation rates (SFR) imply [49] that the observed heavy element abundances are reached after only a few million years. This clearly suggests that what we are witnessing in these galaxies are *starbursts*, that is, short periods of intense star formation. Another strong hint that these galaxies are undergoing starbursts is that continuous star formation at the present SFR would have stripped most BCDs of their HI gas in a time scale of  $10^7$  to  $10^{10}$  years [15]. Moreover, studies of their spectral energy distributions have shown that they display a strong UV continuum, steeply rising towards the blue, a feature indicative of the formation of O and

---

<sup>1</sup>This can be somewhat “relaxed”, given the possibility for galactic winds to expel heavy elements or for infalling gas to dilute them, thus causing a drop in metallicity.

B stars [15] which quickly fades away when star formation ceases<sup>2</sup>. This suggests that two types of dwarfs (Blue Compact Dwarfs and dwarf Irregulars) are actually two possible states for a single class of objects, BCDs being the active, star forming counterparts of quiescent dIs. Indeed, Thuan [45, 46] showed that the majority of BCDs had underlying red components, which were similar to the stellar population of dIs and could well be interpreted as old stars formed in earlier bursts<sup>3</sup>. It will be one of our purposes here to check on this hypothesis.

The most widely accepted physical mechanism for sustaining starbursts in dwarf galaxies is called “self-propagating star formation” (SPSF). It was first devised as a stochastic, merely computational model (see for example [19, 8, 9]) but many later studies have come to support the hypothesis that star formation at a given location produces a disturbance in the local gas through stellar winds and - more importantly - supernovae, causing the collapse of nearby HI clouds and the formation of new stars. For example, BCDs frequently exhibit “superbubble blowouts” [33], with giant HII regions where the gas is ionized by photons from hot, young stars. There is also evidence of more evolved stellar populations downstream from current star-forming regions.

### 1.1.4 Rotational versus chaotic motions

Another major difference between dwarf and spiral galaxies is that most dwarfs are not rotationally dominated. Quantitatively, this means that the ratio of the rotational velocity,  $V_{rot}$ , to the velocity dispersion,  $\sigma$ , is less than or comparable to unity. As a result, and as Staveley-Smith *et al.* [40] put it : “on average, dwarf galaxies are fat, not flat objects” (see also [3]). They might therefore prove more difficult to model, kinematically and dynamically, than the regular, rotating disks of spiral galaxies.

### 1.1.5 Our sample

We present here a brief introduction to the four objects studied in this work. A summary of their properties is given in Table 1.1.

#### NGC 2366

NGC 2366 is a magellanic irregular, in the M81 group. Both in its appearance and its properties, it is quite similar to the Large Magellanic Cloud (LMC), and the southwest part of the galaxy displays a 30 Doradus-like HII region surveyed by Markarian (MK 71). These features can be seen in the Digitized Sky Survey (DSS) images shown in fig. 2.2. Aparicio *et al.* [2] have provided a photometric study of resolved stars in NGC 2366. A previous HI observation by Wevers [51] with the Westerbork Synthesis Radio Telescope has shown that NGC 2366 displays no spiral pattern in its gas distribution.

#### I Zw 49

I Zw 49 (also known as NGC 4861, Arp 266 and Markarian 59) bears considerable optical resemblance to NGC 2366. It is a “comet galaxy”, with bright knots scattered along the north-south axis of an underlying diffuse galaxy (which is known as IC 3961). The brightest of these knots is at the extreme south of the object and, according to Kennicutt *et al.* [24], its  $H\alpha$  flux is 6 times larger than that of 30 Doradus in the LMC. In the same work, they have identified 27 HII regions in this system.

---

<sup>2</sup>Since only a small number of short starbursts are “allowed” given these constraints, it might be that some of these galaxies have never undergone any previous star formation episode, in which case they would be considered pristine. It is argued that I Zw 18 is such an object.

<sup>3</sup>This is to be taken with a little salt, since it is not easy to discriminate between old giants and young red supergiants stars.

## VII Zw 403

VII Zw 403 belongs to the morphological type iE presented in [27], which indicates an irregular star-forming center superimposed on an elliptical low surface brightness object. Schulte-Ladbeck, Crone & Hopp [35] have shown that the red color of the underlying galaxy suggested the presence of an old stellar population. VII Zw 403 would therefore not be a pristine object.

## Haro 2

A good introduction to Haro 2 can be found in Loose & Thuan [28]. It is classified as nE, indicating a bright central star-forming nucleus (n) surrounded by an elliptical (E) distribution of low surface brightness material. Loose and Thuan argue that despite the fact that this class of objects is quite small (encompassing one BCD out of five), it is nevertheless very interesting because of the simple structure that these galaxies harbor, and because “they may present the most extreme examples of ellipticals presently undergoing star formation”.

Parameters	NGC 2366	I Zw 49	VII Zw 403	Haro 2	Ref.
Type	IB(s)m	IB(s)m	Pec	Im Pec	NED <sup>1</sup>
$\alpha$ (J2000)	07h28m54.96s	12h59m01.78s	11h28m00.40s	10h32m31.93s	NED
$\delta$ (J2000)	69d12m56.6s	34d51m39.7s	78d59m35.9s	54d24m03.5s	NED
$l_{galactic}$ (deg)	146.42	11.52	127.84	156.20	[12]
$b_{galactic}$ (deg)	28.54	82.10	37.33	52.80	[12]
$V_H$ (km.s <sup>-1</sup> )	96	847 <sup>2</sup>	-92	1454	[44]
$D$ (Mpc)	3.54	7.2	4.5 <sup>3</sup>	20.5	[44]
$i$ (deg)	65.7	71.2	55.7	0.0	[44]
$D_{25}$ (")	487.7	238.9	86.7	60	[12]
$r_{25}$	0.41	0.37	0.57	0.93	[12]
$B_T^0$	10.95	12.17	14.10	13.38	[12]
$M_{B_T}^0$	-16.79	-17.12	-14.17	-18.18	[12]
$L_B$ (10 <sup>9</sup> L <sub>⊙</sub> )	0.81	1.09	0.072	2.91	[12]
$\Delta V_{50}$ (km.s <sup>-1</sup> )	99	92	43	113	[44]
$\Delta V_{20}$ (km.s <sup>-1</sup> )	126	125	54	153	[44]
$S_H$ (Jy.km.s <sup>-1</sup> )	202.6	31.8	14.32	4.36	[44]

Table 1.1: Parameters for our objects, including position in equatorial and galactic coordinates, heliocentric systemic velocity, distance, inclination on the line of sight, optical dimensions (diameter  $D_{25}$  and ratio  $r_{25}$  of minor to major axis, measured at the 25 mag.arcsec<sup>-2</sup> isophote), B Band photometry and HI observations.

<sup>1</sup>NED is the NASA/IPAC Extragalactic Database (<http://nedwww.ipac.caltech.edu>).

<sup>2</sup>From [16].

<sup>3</sup>From Lynds, Tolstoy, O’Neil, & Hunter (in print).

## 1.2 Physical principles of interferometry

This introduction to interferometry is primarily based on the excellent proceedings of the third NRAO Synthesis Imaging Summer School held at Socorro in June 1988 [7, 11, 17, 32, 39, 42].

### 1.2.1 Propagation of information

Information on an astrophysical phenomenon occurring at location  $\mathbf{R}$  is primarily obtained through the measurement, by an observer at  $\mathbf{r}$ , of the resulting electromagnetic emission. To simplify the equations, we shall take into account the sole electric field  $\mathbf{E}(\mathbf{R}, t)$ , given that the magnetic field can then be derived from Maxwell's theory. For further simplification, we shall consider only one component of the field, thus formally supposing it to be scalar. Due to the linearity of Maxwell's equations, we can also avoid the trouble of a time-dependent observed field  $E(\mathbf{r}, t)$  by considering only the (complex) *quasi-monochromatic components*  $E_\nu(\mathbf{r})$

$$E(\mathbf{r}, t) = \frac{1}{\sqrt{2\pi}} \int_0^\infty E_\nu(\mathbf{r}) e^{2i\pi\nu t} d\nu. \quad (1.1)$$

Furthermore, the same linearity allows us to simply superpose the fields produced at the observer's location by the various source points

$$E_\nu(\mathbf{r}) = \iiint \mathcal{P}_\nu(\mathbf{R}, \mathbf{r}) E_\nu(\mathbf{R}) d^3\mathbf{R}, \quad (1.2)$$

where  $\mathcal{P}_\nu(\mathbf{R}, \mathbf{r})$  is the *propagator function*. Given the “astronomical” distance of the source, we cannot hope to describe its structure in the third dimension. More precisely, what we can measure is its *surface brightness distribution*

$$\mathcal{E}_\nu(\mathbf{n}) = \int E_\nu(\mathbf{R}) d|\mathbf{R}|, \quad (1.3)$$

where we have integrated along the line of sight of unit vector  $\mathbf{n} = \mathbf{R}/|\mathbf{R}|$ .

It is convenient to think of our source as projected onto a “celestial sphere” of radius  $|\mathbf{R}|$ . If we assume that there is no other emission within this sphere, the Huygens-Fresnel Principle yields a simple form for the propagator, and (1.2) becomes

$$E_\nu(\mathbf{r}) = \iint \mathcal{E}_\nu(\mathbf{n}) \mathcal{A}_\nu(\mathbf{n}) \frac{e^{2i\pi\nu|\mathbf{R}-\mathbf{r}|/c}}{|\mathbf{R}-\mathbf{r}|} dS. \quad (1.4)$$

In this equation,  $\mathcal{A}_\nu(\mathbf{R})$ , called the *primary beam*, takes into account the fact that antennae are not point probes, but have a direction-dependent sensitivity. It is therefore a function falling rapidly to zero except in the immediate vicinity of a certain direction, usually called the *phase tracking center*, where it takes the value of unity. We will also suppose that all antennae in a given array have the same primary beam.

### 1.2.2 The spatial coherence function

The purpose of an interferometer is to measure the correlation between the fields at different locations, say  $\mathbf{r}_1$  and  $\mathbf{r}_2$ , through the *spatial coherence function*<sup>4</sup>

$$V_\nu(\mathbf{r}_1, \mathbf{r}_2) = \langle E_\nu(\mathbf{r}_1) E_\nu^*(\mathbf{r}_2) \rangle. \quad (1.5)$$

---

<sup>4</sup> $V$  stands for “visibility”.



Here,  $\langle . \rangle$  is a statistical expectation and  $*$  stands for complex conjugation. Using (1.4), and assuming that the various source points are uncorrelated,

$$V_\nu(\mathbf{r}_1, \mathbf{r}_2) = \int \langle |\mathcal{E}_\nu(\mathbf{n})|^2 \rangle |\mathbf{R}|^2 \mathcal{A}_\nu^2(\mathbf{n}) \frac{e^{2i\pi\nu|\mathbf{R}-\mathbf{r}_1|/c}}{|\mathbf{R}-\mathbf{r}_1|} \frac{e^{-2i\pi\nu|\mathbf{R}-\mathbf{r}_2|/c}}{|\mathbf{R}-\mathbf{r}_2|} dS. \quad (1.6)$$

Eventually, since  $|\mathbf{r}| \ll |\mathbf{R}|$ , we have a very simple expression of  $V_\nu(\mathbf{r}_1, \mathbf{r}_2)$ , featuring the observed intensity  $I_\nu(\mathbf{n}) = \langle |\mathcal{E}_\nu(\mathbf{n})|^2 \rangle |\mathbf{R}|^2$

$$V_\nu(\mathbf{r}_1, \mathbf{r}_2) = \int I_\nu(\mathbf{n}) \mathcal{A}_\nu^2(\mathbf{n}) e^{-2i\pi\nu\mathbf{n} \cdot (\mathbf{r}_1 - \mathbf{r}_2)/c} d\Omega. \quad (1.7)$$

The important thing to note here is that  $V_\nu(\mathbf{r}_1, \mathbf{r}_2)$  does not depend on the absolute values of  $\mathbf{r}_1$  and  $\mathbf{r}_2$ , but only on the *baseline*  $\mathbf{r}_1 - \mathbf{r}_2$ . Furthermore, since the primary beam correction is a mere division that can be done at the end of the data reduction process, we will simplify our notations by defining

$$J_\nu(\mathbf{n}) = I_\nu(\mathbf{n}) \mathcal{A}_\nu^2(\mathbf{n}). \quad (1.8)$$

### 1.2.3 Synthesis imaging through Fourier transforms

Of course, what we are now seeking is an inversion of equation (1.7) to obtain the intensity  $I_\nu(\mathbf{n})$ . This can be done in a special case we will assume from now on. Let us suppose that the source we wish to observe is limited to a small portion of the sky around the phase tracking center  $\mathbf{n}_0$ . Hence  $\mathbf{n} = \mathbf{n}_0 + \delta\mathbf{n}$  with  $|\delta\mathbf{n}| \ll 1 = |\mathbf{n}_0|$ , and it is obvious that  $\delta\mathbf{n} \cdot \mathbf{n}_0 = 0$ . In a proper coordinate system,  $\mathbf{n}_0 = (0, 0, 1)$  and  $\mathbf{r}_1 - \mathbf{r}_2 = \lambda(u, v, w)$  ( $\lambda$  being the wavelength). Equation (1.7) then gives

$$V'_\nu(u, v, w) = e^{-2i\pi w} \iint J_\nu(l, m) e^{-2i\pi(ul+vm)} dl dm, \quad (1.9)$$

where  $l$  and  $m$  are the sky coordinates that  $\mathbf{n}$  points to. It is usual to have the exponential factor absorbed by the visibility function, so that we may consider the function of two variables

$$V_\nu(u, v) = e^{2i\pi w} V'_\nu(u, v, w) = \iint J_\nu(l, m) e^{-2i\pi(ul+vm)} dl dm. \quad (1.10)$$

This is a simple Fourier transform relation, easily inverted

$$J_\nu(l, m) = \iint V_\nu(u, v) e^{2i\pi(ul+vm)} du dv. \quad (1.11)$$

### 1.2.4 The problem of deconvolution

#### Never enough data !

Unfortunately, the spatial coherence function is not known everywhere in the  $u-v$  plane (see fig. 1.1), but only at certain points, since we have but a finite number of antennae and a limited observation time. We can describe this effect by introducing a *weighted sampling function*  $S(u, v)$  that is non-zero only at these points

$$S(u, v) = \sum_k D_k \delta(u - u_k, v - v_k). \quad (1.12)$$

The *density weights*  $D_k$  will be discussed at the end of this section.

Now, if we perform the inversion as we did before, the function we obtain is not the true intensity  $J_\nu(l, m)$ , but what radioastronomers call the *dirty image*:

$$J_{\nu}^D(l, m) = \iint V_{\nu}(u, v) S(u, v) e^{2i\pi(ul+vm)} du dv. \quad (1.13)$$

If we introduce the *synthesized beam*

$$B(l, m) = \iint S(u, v) e^{2i\pi(ul+vm)} du dv, \quad (1.14)$$

it is clear that we have a convolution relation :

$$J_{\nu}^D = J_{\nu} * B. \quad (1.15)$$

Most of the data reduction process will therefore reside in a deconvolution.

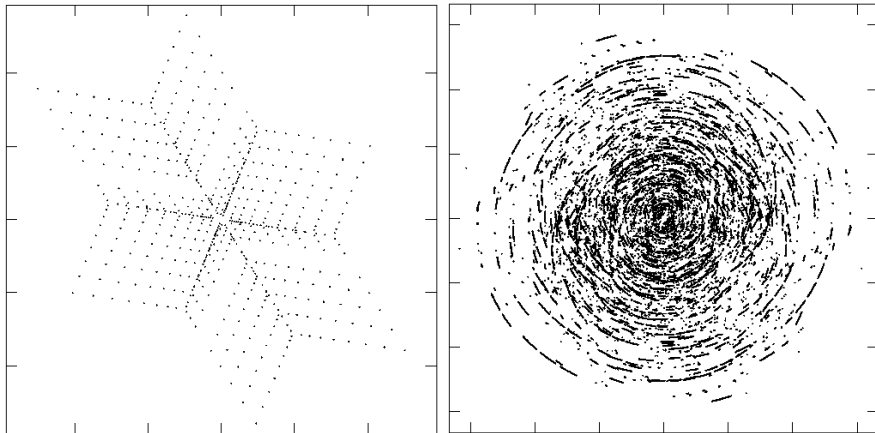


Figure 1.1: 1-minute “snapshot” (left) and our  $u$ - $v$  coverage in the observation of NGC 2366 (right).

## The model approach

However, “classic” linear deconvolution [1] would be of no use in this case, since with a finite number of data points in the  $u - v$  plane, we could not hope to recover the intensity  $J_{\nu}$ .

It is preferable to construct a model,  $\hat{J}_{\nu}$ , to approximate the true intensity. Obviously, our first clue as to whether our model is convincing or not should be that, convolved with the dirty beam, it yields the dirty image. It should be emphasized here that there is no unique solution  $J_{\nu}$  to (1.15). If  $Z$  is a solution to the homogeneous equation  $B * Z = 0$ , then  $J_{\nu} + Z$  is also a possible answer to our problem. Such *invisible distributions*  $Z$ , as can be deduced from equation (1.13), are Fourier transforms of functions  $W(u, v)$  with  $WS = 0$ . The solution to the convolution equation having zero amplitude outside of the sampled  $u - v$  points is called *principal solution*, although it seldom represents the true intensity, being often hampered by unphysical features and low stability [11]. “Deconvolution” algorithms are actually programs providing physically believable model intensities that are solutions to (1.15).

## The CLEAN algorithm

CLEAN - implemented in the *AIPS* task IMAGR - is probably the most commonly used of those algorithms. It was first devised by Högbom [21], and then most notably improved by Clark [6] and Cotton and Schwab [36]. Its working is quite simple [11]: First of all, it finds the position and strength of the peak intensity in the dirty map<sup>5</sup>, then multiplies its strength by a *loop gain* factor. The result,

<sup>5</sup>or in only parts of it called CLEAN *boxes*.

a  $\delta$ -function called a CLEAN *component*, is convolved with the dirty beam and subtracted from the dirty image. The procedure continues until there is no remaining peak above a certain user-defined flux level, or a user-defined number of iterations is reached. The CLEANed image is eventually the sum of the CLEAN components, convolved with an elliptical Gaussian called the CLEAN *beam*. The size of the CLEAN beam is chosen to reflect the finite resolution of the array. Also, some programs add the residuals of the dirty image. The shape of the dirty beam, and consequently the CLEANed image, obviously depends on the choice of the density weights  $D_k$  introduced in, for which we have two main possibilities : *Natural weighting*, with  $D_k = 1$ , and *uniform weighting*, with  $D_k = 1/N_k$ . Uniform weighting tries to compensate for the fact that the density of sampled points varies in the  $u - v$  plane.  $N_k$  is therefore the number of such points in a given area around the  $k^{th}$  visibility. In VLA observations, the  $u-v$  coverage is denser around the short baselines (see fig. 1.1). As a result, natural weighting will emphasize shorter spatial frequencies than uniform weighting. In return, since uniform weighting emphasizes longer spatial frequencies, it will have a better resolution. In between those two extremes, Daniel Briggs' robustness parameter<sup>6</sup> allows a number of possible weightings for the user to trade off sensitivity with resolution [5].

A final word of introduction to radio interferometry : if you would like to get a “hands-on” experience of how all of this works, I encourage you to visit the ATNF's “Virtual Radio Interferometer”, at <http://wwwnar.atnf.csiro.au/astronomy/vri.html>. It is a Java applet showing how one gets from an array to the corresponding  $u - v$  coverage, and what Fourier transforms of radio images look like. Below is a screenshot from this applet.

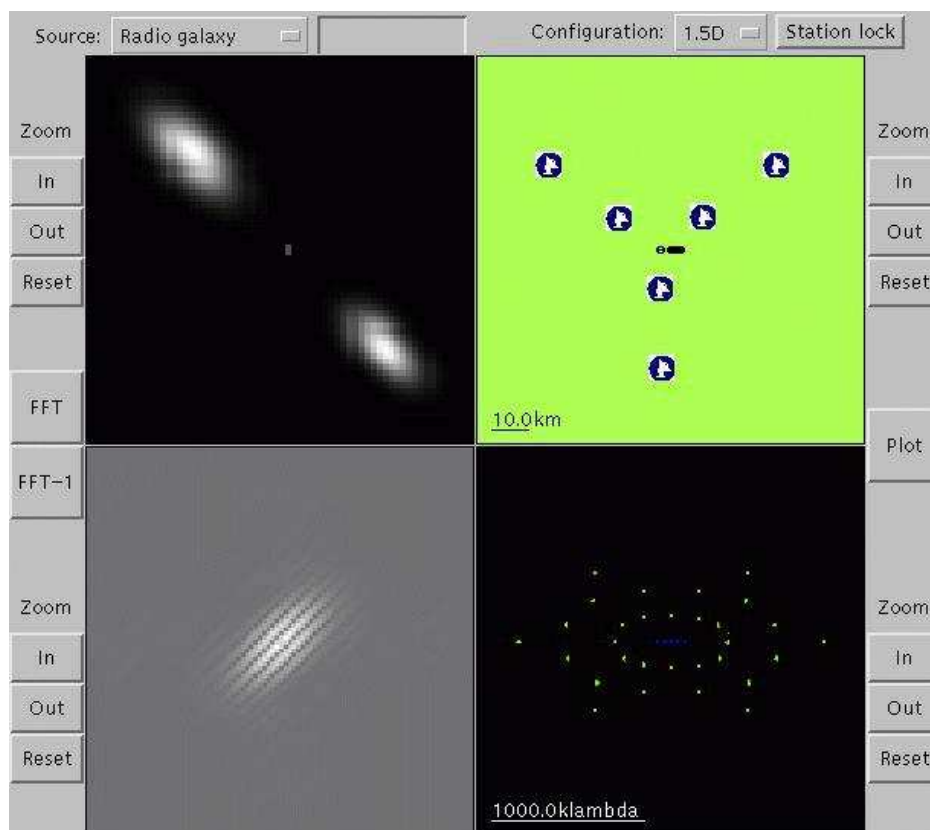


Figure 1.2: A screenshot from the “Virtual Radio Interferometer”.

<sup>6</sup>IMAGR's ROBUST adverb.

## 1.3 Spectral line imaging

### 1.3.1 Definition of a spectral line

We will talk of a *spectral line* as a higher intensity feature in the spectrum of a source, whose width is much less than its central frequency. Mathematically, the spectral energy distribution of the source is given by

$$S(\nu) = S_c + S_l(\nu, \nu_0, A, \Delta\nu), \quad (1.16)$$

where  $S_c$  is the *continuum emission* and  $S_l$  is the *line emission* proper, both measured in Janskys ( $Jy$ ).  $S_c$  usually varies slowly with frequency, so we can consider it constant over the narrow bandwidths we will deal with.  $S_l$  is characterized by its amplitude<sup>7</sup>  $A$ , its central frequency  $\nu_0$ , and its width  $\Delta\nu$  (for example the full width at half-maximum - FWHM).

### 1.3.2 The neutral hydrogen line

In a neutral hydrogen atom, if the spins of the proton and the electron are parallel, there is a probability that the electron will “flip” in order to achieve a lower energy state, resulting in the emission of a 1420.405752 MHz photon. Even though this probability is very low, the number of HI atoms in the Universe is unconceivably large, making this line fully visible in many objects.

### 1.3.3 The Doppler effect

What is the use of observing such a line ?

It is well-known that the observed frequency  $\nu$  of an electromagnetic wave differs from the emission frequency  $\nu_0$ , due to the relative radial velocity  $v$  of the source and the observer<sup>8</sup>. Through the relativistic expression

$$v = c \frac{\nu_0^2 - \nu^2}{\nu_0^2 + \nu^2} \quad (1.17)$$

it is then possible to derive  $v$  from the shift in frequency<sup>9</sup>. The purpose of spectral line imaging is now clear : to describe the kinematics of an object using the Doppler effect. This requires observing a source at a number of different frequencies, so that the final product of a spectral line observing run is a 3-dimensional *cube* of intensities  $I(l_i, m_j, \nu_k)$  at each pixel  $i, j, k$ . That is, a set of two-dimensional<sup>10</sup> images at each frequency  $\nu_k$ .

### 1.3.4 Cubes and moments

The cubes are the first visible result of an observing run. They can be viewed in various ways, including playing them as movies or displaying them in 3 dimensions as is done in KARMA’s XRAY. Each plane of the cube being an image of the emission at a given velocity  $v_k$  deduced from the frequency  $\nu_k$  via (1.17), it is quite straightforward to compute the moments of the gas distribution.

---

<sup>7</sup>A can be negative, in which case, we have an *absorption line*...

<sup>8</sup>that is, the relative velocity projected onto the line of sight.

<sup>9</sup>Note that astronomers use *two* different approximations of equation (1.17), in the limit  $v \ll c$ , called the *optical* and *radio* velocities, and also that physical consistency of derived velocities requires corrections for the motions of the Earth around its axis and the Sun, of the Sun around the Galaxy, etc...

<sup>10</sup> $l$  and  $m$  are the coordinates introduced in **1.2.3**.

Moment 0, which represents the total emission and for which we have, at each pixel<sup>11</sup>:

$$I_0(l_i, m_j) = \sum_k I(l_i, m_j, v_k) \quad (1.18)$$

Moment 1, which yields the intensity-weighted velocity field :

$$v(l_i, m_j) = \frac{1}{I_0(l_i, m_j)} \sum_k v_k I(l_i, m_j, v_k) \quad (1.19)$$

And moment 2, representing the velocity dispersion :

$$\sigma(l_i, m_j) = \sqrt{\sum_k \frac{v_k^2 I(l_i, m_j, v_k)}{I_0(l_i, m_j)} - v^2(l_i, m_j)} \quad (1.20)$$

## 1.4 The Very Large Array

The Very Large Array (VLA), located in Socorro, in the desert of New Mexico, is the largest radio astronomy facility in the world. The VLA consists of 27 antennae, each 25 meters in diameter, arranged in a Y pattern [30]. The antennae can be moved on railway tracks to be cycled through four configurations (A, B, C and D) in 15 months. The purpose of this cycle is to allow different spacings and therefore different sensitivities and resolutions, from A configuration, the largest one (the longest baseline being 36 km), which has hence the best resolution but lowest sensitivity to extended emission, through D configuration, the most compact one, which trades better surface brightness sensitivity for a lesser resolution. Our observations were all made with the VLA in its C configuration, in 1984, 1986 and 1992. The observing parameters are given in table 1.2 below.



**Figure 1.3:** The VLA in D configuration

Parameters	NGC 2366	I Zw 49	VII Zw 403	Haro 2
Date	04/23/1984	04/11/1992	04/11/1992	10/27/1986
Configuration	C	C	C	C
Correlator mode	2A	2AC	2AC	2A
Number of antennae	25	27	27	27
Time on source (min)	538	266	226	456
Flux calibrator	3C286	1328+307	1328+307	3C286
Phase calibrator	071+439	1328+307	1039+811	1031+567

Table 1.2: Observing parameters.

<sup>11</sup>Since a threshold usually applies in order to get rid of the noise and that data is also smoothed during the process, equations (1.18), (1.19) and (1.20) are only approximations.

# Chapter 2

## The analysis and the results

### 2.1 Data Reduction using the *AIPS* package

#### 2.1.1 Introduction

The Astronomical Image Processing System (*AIPS*) is a set of tasks written by the National Radio Astronomy Observatory (NRAO) in order to perform the reduction and analysis of radio-interferometry data. *AIPS* is not a trivial package, and I would never have been able to learn even its main features, had it not been for John Hibbard's constant help and the easy-to-follow instructions given in the *Step-by-Step Guide to Spectral-Line Data Analysis in AIPS*. We also sometimes referred to the *AIPS Cookbook* for a more detailed explanation of a specific task.

#### 2.1.2 Edition and Calibration

The reduction process starts with a careful editing of the data, flagging unlikely high points or bad scans. For this, we used the interactive task TVFLG. Such discrepant, unphysical points can for example be attributed to interference from the ground<sup>1</sup>. When satisfied with the result, we proceeded to the calibration of our data sets to determine the complex gains of the antennae during the observations.

First, the task SETJY calculates the theoretical flux of the primary calibrator, and the procedure VLACALIB determines the relative gains and phases of the antennae for all calibrators. There, possible errors are reported, prompting users to re-edit the data. With this done, the task GETJY is run to bootstrap the fluxes of secondary calibrators, and the results are compared with those tabulated in the VLA Calibrator Manual. Procedure VLACLCAL then interpolates the gain and phase solutions for all sources throughout the observation. The calibration process then ends with that of the bandpass, using the task BPASS. The resulting plots are shown in fig. 2.1. Bandpasses for VII Zw 403 and I Zw 49 are actually the same, since these two objects were observed during the same run, and this bandpass is quite typical of what one would expect. Now, even though Haro 2's may seem strange, we can see that its variations are insignificant (1/1000 or so), so we felt no need to re-edit the data here. An interesting feature is the fall-off at the end of NGC 2366's bandpass, which - given the velocity at which it occurs - can be attributed to galactic HI absorption. The suspect channels were therefore not used in later stages, and neither were the first and last few channels in each observation, as they might be hampered by the rise and fall of the bandpass.

All calibration and editing tables are then applied to our data using the task SPLIT, which also breaks multi-source files (calibrator and program sources) into single-source ones.

---

<sup>1</sup>especially if the source's position requires the antennae to be low on the horizon.

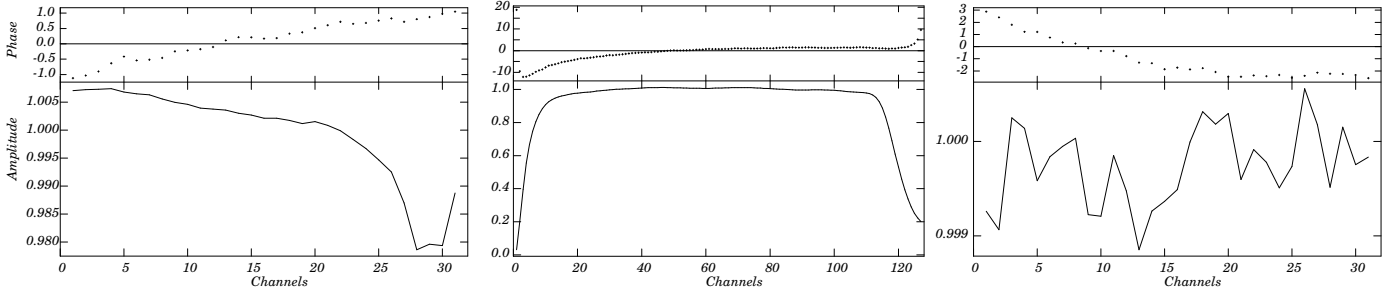


Figure 2.1: The bandpasses. From left to right : NGC 2366, I Zw 49 and VII Zw 403, Haro 2.

### 2.1.3 Imaging

The first run of the main imaging task in *AIPS*, called IMAGR, yields “dirty” data cubes, and a CLEAN algorithm is then used to perform the deconvolution discussed in 1.2.4. Dirty cubes are nevertheless useful to detect problems in the data that could have been overlooked during the editing process. Users can then go back and carefully re-edit the data<sup>2</sup>. Moreover, line-free channels in these cubes are properly averaged to make a continuum map of the field<sup>3</sup>, which is then subtracted from the cube using the task UVLIN. The new, continuum-free cube is then CLEANed via IMAGR. It is at this stage that one can set the ROBUST parameter in order to achieve various weightings of the data and therefore various sensitivities and resolutions. We chose to make three cubes per object, the characteristics of which (channel spacing, pixel size, CLEAN beam size, number of pixels per beam and sensitivity) are listed in table 2.1. The first cube, using  $R = -1$ , allows for a greater resolution (as can be seen from the fact that it has a smaller beam) but ignores faint extended structures (as can be deduced from its surface brightness sensitivity). These “high resolution” cubes will be useful to determine the kinematics our objects. A second cube, using  $R = 1$  trades a lesser resolution for better sensitivity. Still, it might miss features with short spatial frequencies. To recover these structures, the  $R = 1$  cubes were smoothed to a low resolution of  $35'' \times 35''$  and also in velocity, which gives more strength to faint features that persist over several channels.

From there, there are various ways to measure the total HI emission from an object, of which we tested three. The first one is a simple measure of the addition of pixel values in the zeroth moment, which itself is supposed to be the sum of our different channels. Now, as was pointed out in 1.3.4, this is not as simple, since, in the process of computing the moments, a threshold applies which is meant to suppress the noise. Obviously, there may be features which are below the noise level but are nevertheless “believable”. This method, which was implemented using tasks IMEAN and TVSTAT in *AIPS*, would simply ignore them.

A second method, widely used in optical astronomy and called *aperture photometry*, consists in the integration of the emission in concentric rings from the center to the outer radius of the object. For this, we made zeroth moments using no cutoff and used task IRING to determine the flux.

The last of our three methods requires integrating the area under the source’s spectrum. We have a number of different channels and can, in each one of them, compute the flux from a user-defined “box” around the emission. We simply have to add those values and multiply the result by the channel spacing. This was done with task ISPEC.

<sup>2</sup>This is how we detected possible galactic emission interference in channels 40-41 for VII Zw 403. We therefore decided not to use these channels in the rest of our analysis.

<sup>3</sup>Actually, these channels provide anchor points for a continuum interpolation, so averaging them is but one of the possible ways to make a continuum map out of them.

Source	Cube	$\Delta v$ (km/s)	$\Delta x$ (")	$\theta \times \theta$ (")	$N_{pix/b}$	$1\sigma$ (mJy/b)
NGC 2366	Robust -1	10.31	4	$12.54 \times 11.52$	10.23	1.1
	Robust 1	10.31	4	$16.56 \times 14.63$	17.16	0.78
	Low resolution	22.09	12	$35 \times 35$	9.64	0.65
I Zw 49	Robust -1	2.59	4	$15.22 \times 11.64$	12.55	1.2
	Robust 1	2.59	4	$18.61 \times 14.48$	19.08	1.1
	Low resolution	7.77	12	$35 \times 35$	9.64	0.9
VII Zw 403	Robust -1	2.58	4	$17.19 \times 10.96$	13.34	1.8
	Robust 1	2.58	4	$21.23 \times 14.45$	21.72	1.3
	Low resolution	11.04	12	$35 \times 35$	9.61	0.5
Haro 2	Robust -1	2.59	4	$14.1 \times 12.93$	12.92	1.2
	Robust 1	2.59	4	$19.15 \times 17.14$	23.24	0.84
	Low resolution	22.3	12	$35 \times 35$	9.64	0.76

Table 2.1: Map parameters

We also mentioned that the smoothed cubes give us a better sensitivity, so we are basically quoting the numbers we obtained from these, but we also give the  $R = 1$  values as a comparison.

## 2.2 NGC 2366

### 2.2.1 Morphology

The HI emission of NGC 2366, summed over the different channels of the  $R = 1$  cube, is shown in fig. 2.2. The most prominent feature of this map is the clumpiness of the HI distribution. There are very distinct peaks and “holes”, which is indicative of a disturbed medium.

According to star formation theories, gas falls in a potential well, collapses under its own gravity and forms stars, so we would expect at least some of the HI density peaks to coincide with NGC 2366’s star forming regions. Comparison of optical and HI images in fig. 2.2 shows this to be approximately true for the HII region MK 71. However, a closer look at this location actually shows that HI and optical peaks are somewhat displaced. This can be explained by the fact that neutral gas in star-forming regions may be ionized or pushed aside by stellar winds [33] and supernovae. There is some evidence for this on the dispersion maps (see 2.2.4). There are also a number of holes in the HI distribution. These might be remnants of multiple supernovae having blown up in the interstellar medium [33].

### 2.2.2 HI flux - comparison with single dish

Our results are listed in table 2.2. Also presented (fig. 2.5) is a plot of the spectra from our  $R = 1$  data, our smoothed data and from Thuan & Martin [44].

Flux determination (Jy.km/s)	Robust=1 data	Smoothed data
Zeroth moment	112.8	135.6
Aperture Photometry	90.8	135.0
Spectrum Integration	112.8	138.4

Table 2.2: Flux values for NGC 2366.

We recover 68% of the raw flux in [44], which is 202.6 Jy.km/s. This is very likely to be due to



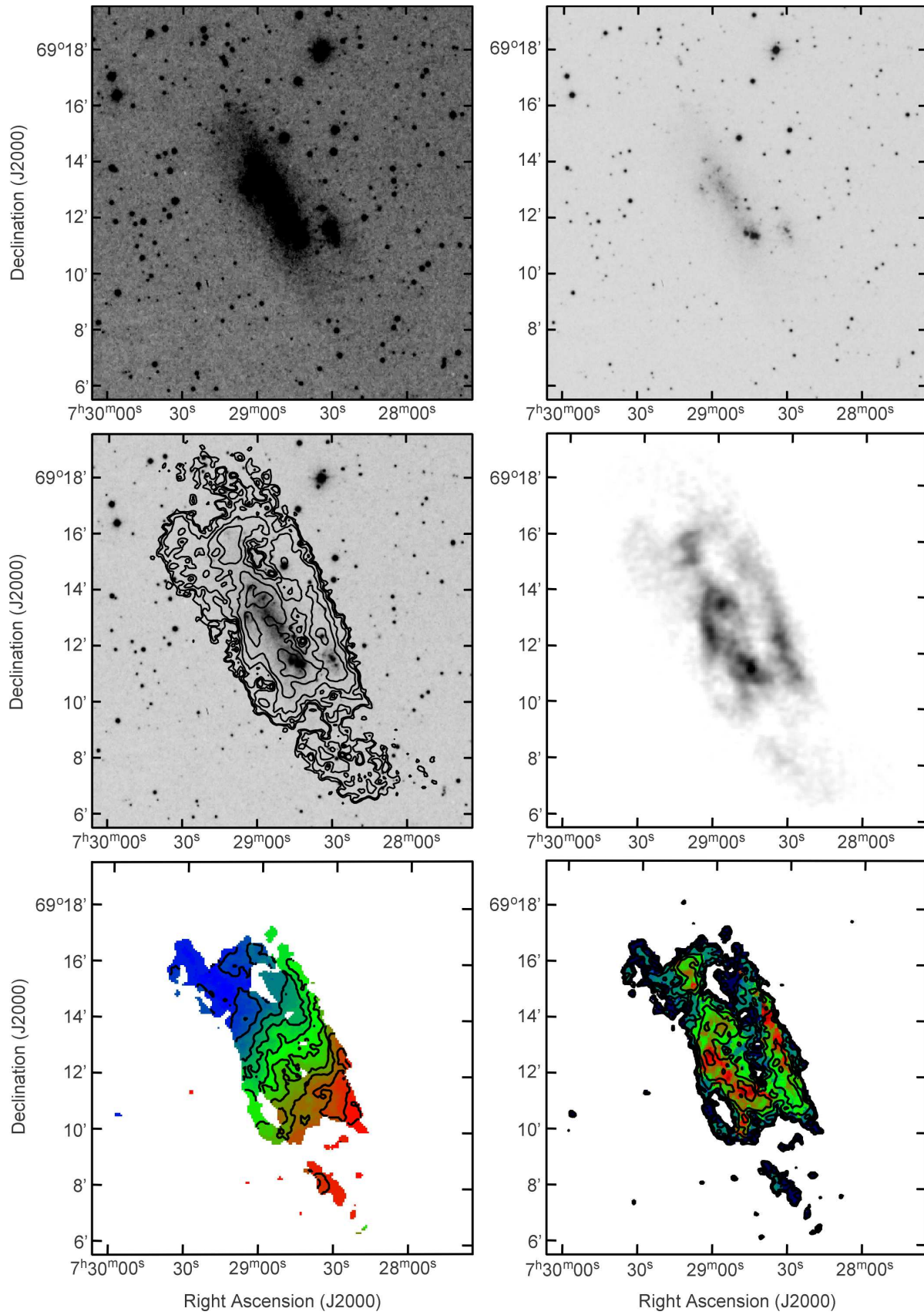


Figure 2.2: NGC 2366. From left to right and top to bottom : DSS showing the extent of the galaxy; DSS showing the star-forming regions; DSS (greyscale) and Moment 0 (contours); Moment 0; Moment 1 (contours and pseudo colours); Moment 0 (contours) and Moment 2 (pseudo colours).

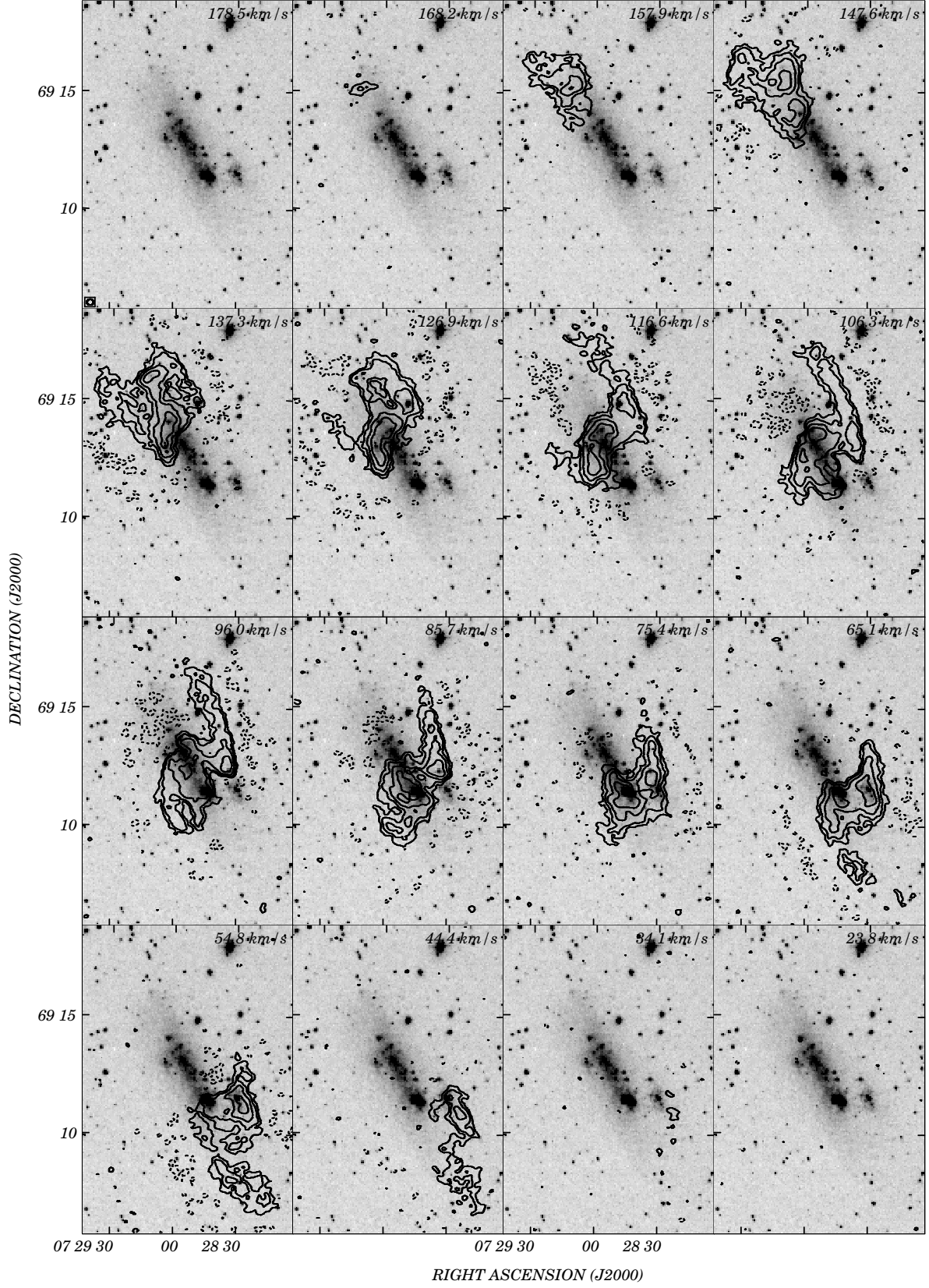


Figure 2.3: Channel maps for NGC 2366 overlaid with the DSS. Contours are  $-1.11 \times 10^{20}$ ,  $1.11 \times 10^{20}$ ,  $2.22 \times 10^{20}$ ,  $4.44 \times 10^{20}$  and  $8.88 \times 10^{20}$  atoms per square centimeter.

faint extended structure that we cannot see with the VLA in this configuration. We miss the short spacings necessary to detect these.

### 2.2.3 Kinematical modeling

NGC 2366’s velocity field, shown in fig. 2.2, shows a number of kinks and bends. In this map, as in the other moment 1 maps, red indicates motion towards us, while blue indicates motion away from us. The most prominent of these features occurs at the northwest end of the galaxy and can also be seen very clearly in the channel maps which show a typical “S” shape, as opposed to the classical “V” shape<sup>4</sup> observed in “normal” spiral galaxies (see e.g. [4]). This feature can be attributed to streaming motions due to the presence of a bar or to the warping of the disk. Nevertheless, we very much believe that NGC 2366’s HI distribution does lie in a disk, and we tried to model its velocity field by fitting a Brandt rotation curve [13]:

$$V(r) = \frac{V_m}{\sin i} \left( \frac{r}{R_m} \right) \left[ \frac{1}{3} + \frac{2}{3} \left( \frac{r}{R_m} \right)^n \right]^{-3/2n} \quad (2.1)$$

where  $V_m$  is the maximum velocity, reached at radius  $R_m$ ,  $i$  is the inclination of the galaxy’s plane on the line of sight and  $n$  is a parameter that sets the shape of the curve.

The output of this fit is a set of geometrical parameters that describe the orientation of the disk, such as the position of the dynamical center, the extent of the galaxy, its inclination, and its position angle with respect to a given axis. The resulting *rotation curve* is shown in fig. 2.4. The solid line is the model curve and the dots represent the deprojected rotational velocity computed from the first moments and the geometrical parameters. The difference between the two curves therefore gives an idea of the residuals. The fit parameters are shown in table 2.3.

$\alpha_0$	$\delta_0$	P.A. (deg)	$i$ (deg)	$V_0$ (km/s)	$V_m$ (km/s)	$R_m$ (arcsec)
7h28m52.39s	69d12m27.82s	50.85	55.95	101.32	66.63	289.91

Table 2.3: Kinematical fit parameters for NGC 2366

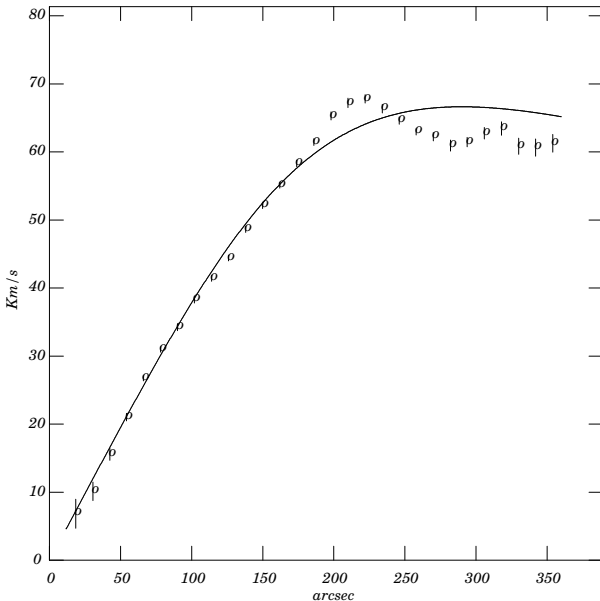


Figure 2.4: Rotation curve for NGC 2366.

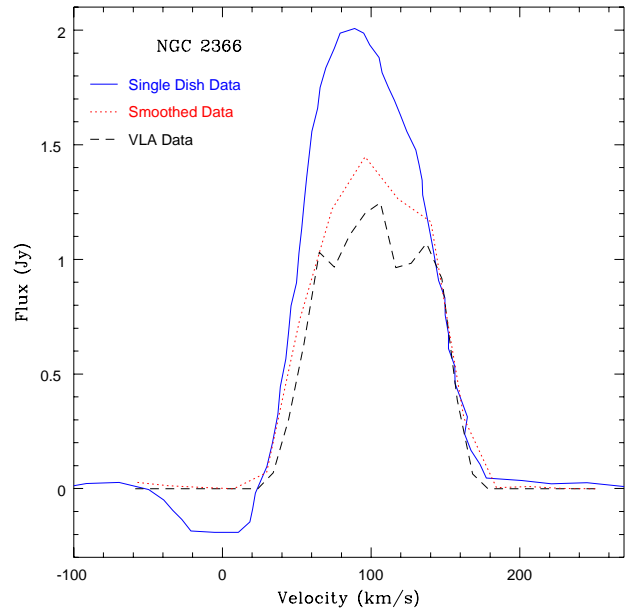


Figure 2.5: Spectra for NGC 2366

<sup>4</sup>or “Butterfly pattern”.

## 2.2.4 Velocity dispersion

The second moment, representing the velocity dispersion, is shown in false colors overlaid with contours of the HI distribution in fig. 2.2. There and in the other moment 2 maps, the velocity dispersion increases from blue to red. It appears quite clearly that the regions with the highest velocity dispersions coincide very well with the density peaks. This is not surprising since the gas in those regions is much more disturbed by shocks and the effects of star formation, and therefore has a larger velocity width. The mean velocity dispersion is  $\sigma = 7.7$  km/s.

## 2.3 I Zw 49

### 2.3.1 Morphology

As with NGC 2366, the total HI emission map for I Zw 49, shown in fig. 2.7, reveals a number of gas clumps which are roughly aligned along a north-south axis. This alignment might be a sign of self-propagating star formation, as described in 1.1.3, although it is believed that SPSF acts on a smaller scale than that of an entire galaxy. There does not seem to be the same kind of “holes” that we found in NGC 2366, however. An interesting feature of this galaxy was found by making a smoothed version of our data cubes, thus gaining better sensitivity to detect faint emission. The resulting HI distribution is shown in greyscale in fig 2.6 (the darker, the more gas rich), along with a contoured version of the original ( $R = 1$ ) zeroth moment. We can see that there is an extended wedge-shaped envelope to the east of the galaxy. It appears to be directed towards an HI cloud, which has no optical counterpart.

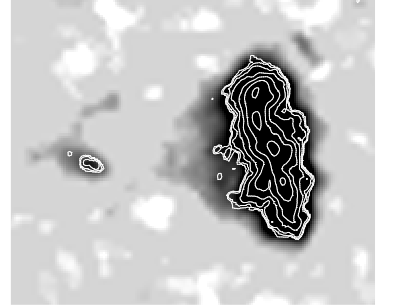


**Figure 2.6:** Overlay of the smoothed and  $R = 1$  zeroth moments for I Zw 49.

It is highly unlikely that this cloud could be pulling material out of the galaxy. In effect, we calculated the masses of both features from the total flux using the equation given in [44]:

$$M_H = 2.36 \times 10^5 D^2 S_H \quad (2.2)$$

where  $M_H$  is the HI mass in solar units,  $D$  is the distance in megaparsecs and  $S_H$  is the flux in Jy.km/s. We find that the HI mass of the cloud is  $M_c \simeq 5.8 \times 10^6 M_\odot$  and that of the envelope approximately  $M_e \simeq 1.1 \times 10^8 M_\odot$ , which yields  $M_e/M_c \simeq 20$ , clearly too much for the envelope to have been pulled out by the HI cloud.

Nevertheless, the fact that the wedge is oriented towards the cloud suggests that these two features may have a common origin. They may be remnants of a previous interaction with a larger object, or may have been expelled by the starbursts. To decide on this we would either need to search for nearby galaxies, use numerical models to determine if the cloud and galaxy’s envelope could be merger remnants, or calculate if the energy released by starbursts in I Zw 49 is sufficient to lift as much as a hundred million of solar masses<sup>5</sup>.

### 2.3.2 HI flux - comparison with single dish

In table 2.4 below are presented the fluxes measured with our three methods. Since Thuan & Martin’s value is 31.8 Jy.km/s, we seem to recover more flux than what they measure.

<sup>5</sup>Taylor (see e.g. [41]) has suggested that, on average, BCDs have an unusually high number of HI companions and that these clouds might actually be triggering star formation in bursting galaxies by “thumping” them.

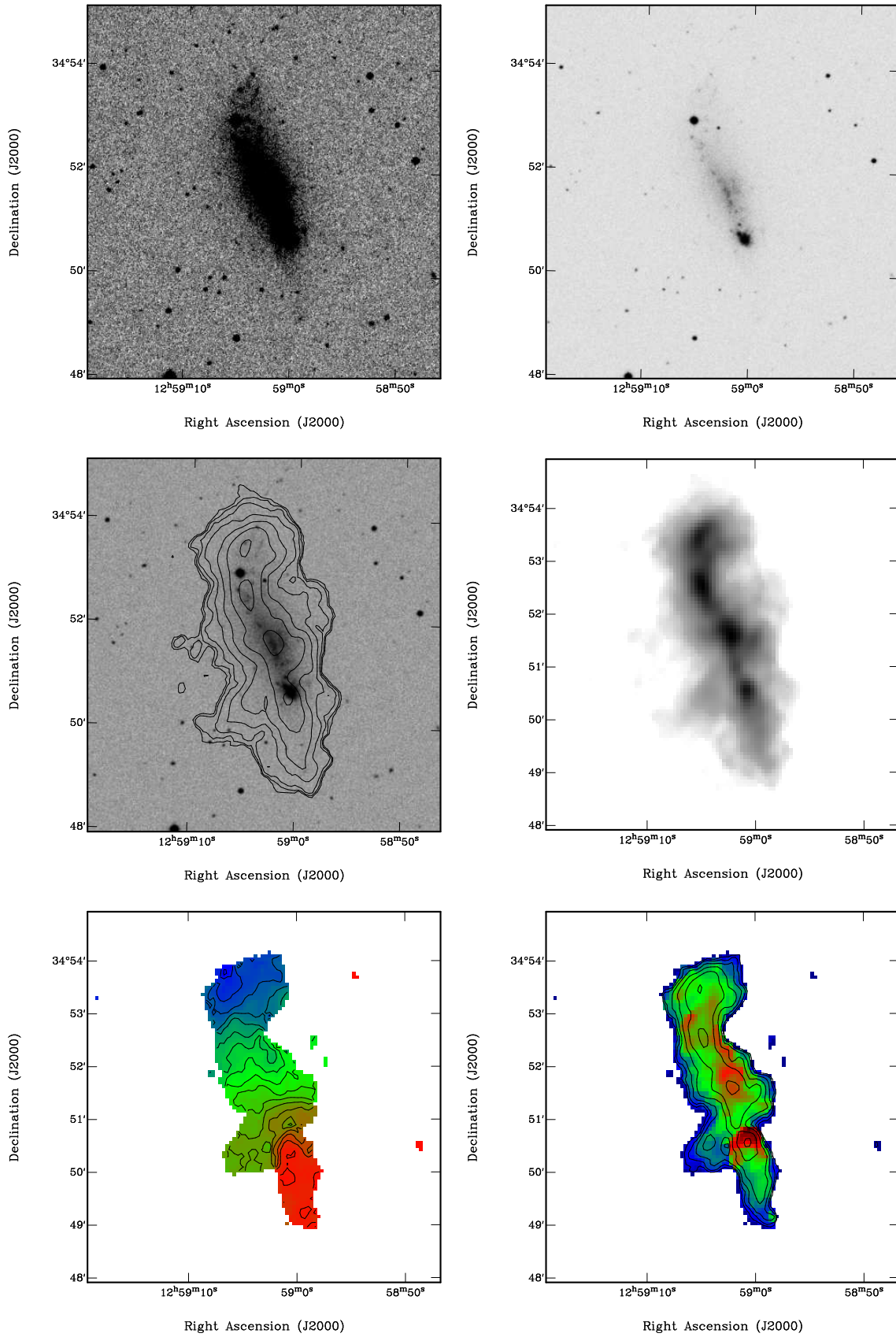


Figure 2.7: I Zw 49. From left to right and top to bottom : DSS showing the extent of the galaxy; DSS showing the star-forming regions; DSS (greyscale) and Moment 0 (contours); Moment 0; Moment 1 (contours and pseudo colours); Moment 0 (contours) and Moment 2 (pseudo colours).

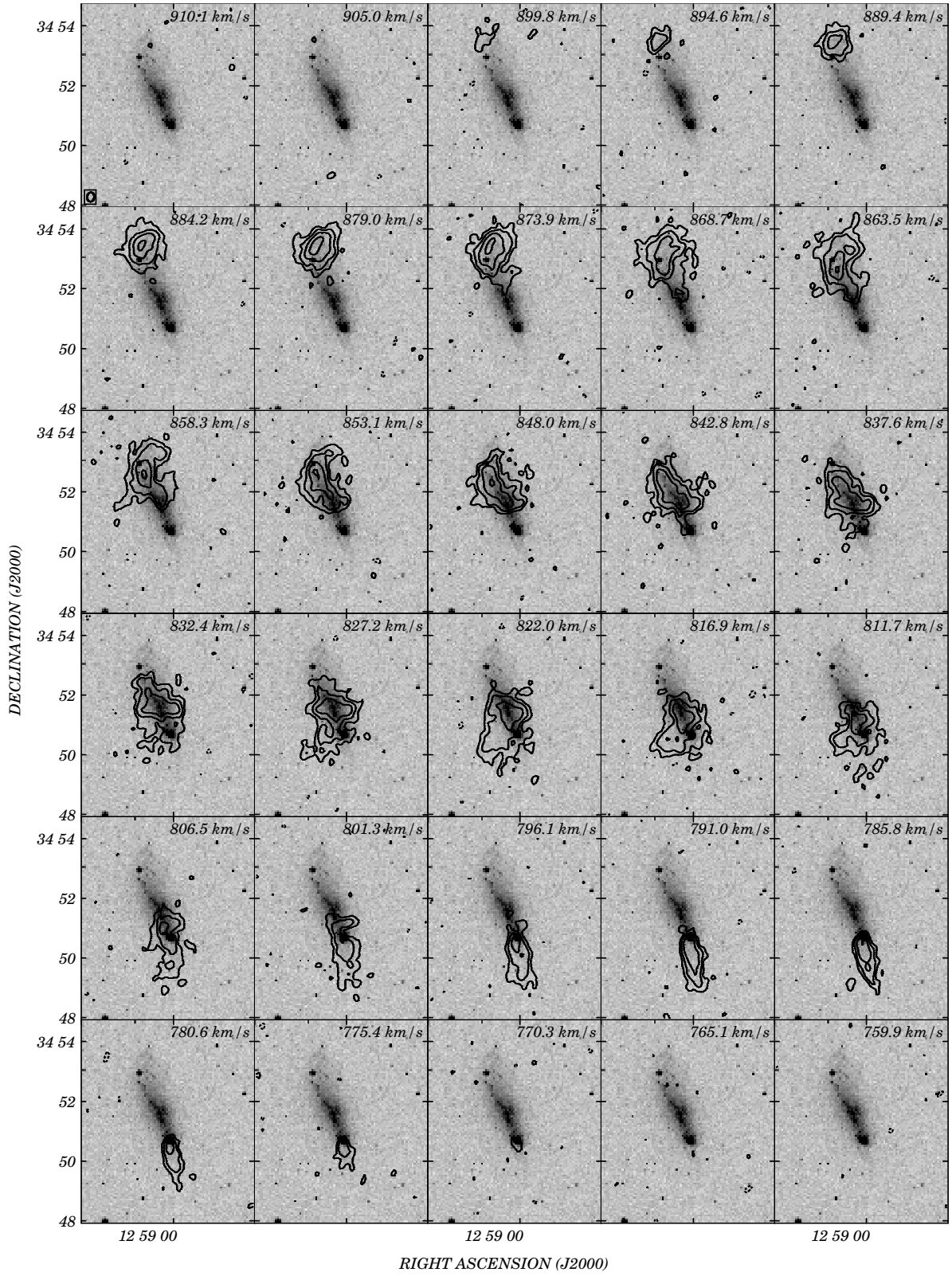


Figure 2.8: Channel maps for I Zw 49. Contours are  $-3.3 \times 10^{19}$ ,  $3.3 \times 10^{19}$ ,  $6.6 \times 10^{19}$ ,  $1.32 \times 10^{20}$  and  $2.64 \times 10^{20}$  atoms per square centimeter.

### 2.3.3 Kinematical modeling

Despite a number of irregularities, the velocity field of I Zw 49 (see fig. 2.7) clearly resembles that of a rotating disk seen almost edge-on. The rotation is also quite obvious in the channel maps (fig. 2.8), where the emission seems to be “moving” from north to south. We used the same method as we did for NGC 2366, and the results are shown in fig. 2.9 and table 2.5.

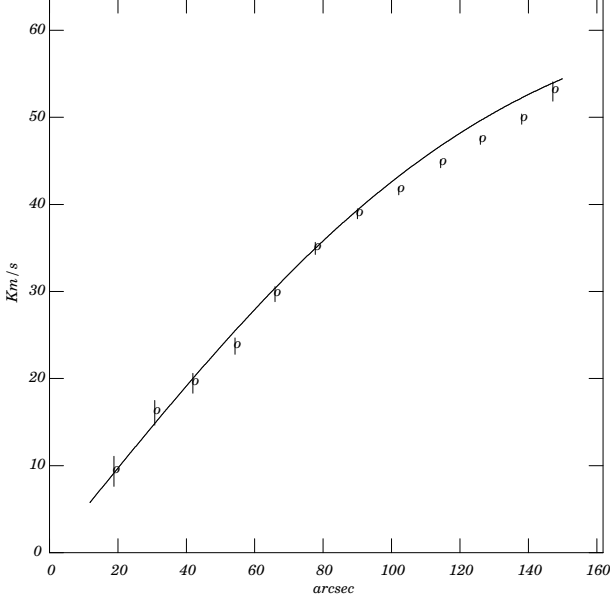


Figure 2.9: Rotation curve for I Zw 49

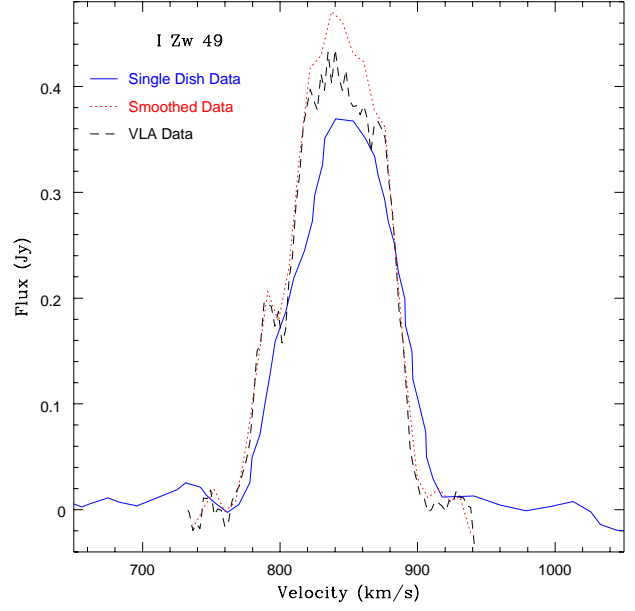


Figure 2.10: Spectra for I Zw 49

Flux determination (Jy.km/s)	Robust=1 data	Smoothed data
Zeroth moment	32.6	38.8
Aperture Photometry	32.9	36.1
Spectrum Integration	35.3	38.4

Table 2.4: Flux values for I Zw 49.

$\alpha_0$	$\delta_0$	P.A. (deg)	$i$ (deg)	$V_0$ (km/s)	$V_m$ (km/s)	$R_m$ (arcsec)
12h59m02.12s	34d51m39.96s	16.82	79.78	833.3	62.21	266.67

Table 2.5: Kinematical fit parameters for I Zw 49

### 2.3.4 Velocity dispersion

The highest peak in the velocity dispersion map (fig. 2.7) - whose mean is  $\sigma = 8.4$  km/s - seems to coincide very well with the star-forming knot to the south of the galaxy. Both are however displaced with respect to the HI peak, as was already noticed for NGC 2366. In fact, the velocity dispersion peak seems to correspond to a minimum of the HI density. We believe this to be due to a faint but very broad line that connects two clumps with quite different velocities. This feature is best seen on the position-velocity profile shown in fig. 2.11 and the resulting broadening of the line accounts for the high velocity dispersion.

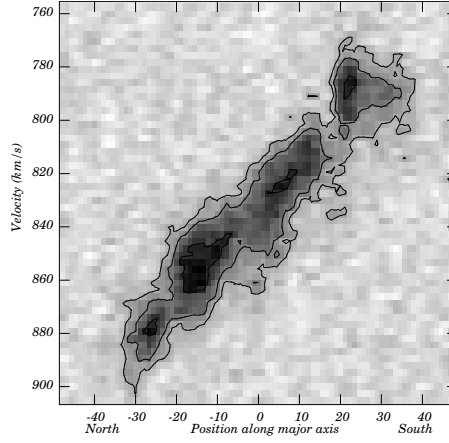


Figure 2.11: Position-velocity profile for I Zw 49. Note the broadening of the line at pos = +20.

## 2.4 VII Zw 403

### 2.4.1 Morphology

If we had to characterize the morphology of VII Zw 403 in one word, this would be “amorphous”. It does look like it is a disturbed medium, however, especially near the edge of the galaxy. We can distinguish two holes to the west and one to the south, as well as a number of filaments all around the object. The most interesting feature of VII Zw 403 is that it appears to be multi-component. This is best seen on the greyscale image of the total HI distribution, in fig. 2.12. There seems to be a second density concentration to the north of the brightest HI peak, which suggests that we might be witnessing the collapse and merging of two distinct objects. There are also hints that support this hypothesis in the channel maps (fig. 2.13), but we cannot be quite positive about it.

### 2.4.2 HI flux - comparison with single dish

As table 2.6 below shows, we have a flux measurement of about 11 Jy.km/s. This is approximately 77 % of Thuan & Martin’s value listed in table 1.1.

Flux determination (Jy.km/s)	Robust=1 data	Smoothed data
Zeroth moment	9.9	11.4
Aperture Photometry	11.1	11.1
Spectrum Integration	11.1	11.0

Table 2.6: Flux values for VII Zw 403

### 2.4.3 Kinematical modeling

The channel maps for VII Zw 403 (fig. 2.13) show evidence of emission over 67 km/s, and the velocity range in the first moment (fig. 2.12) is only 29 km/s. This is much less than for any other of our objects, and it is comparable to the velocity dispersion in this galaxy, as will be discussed in the next paragraph. We modeled VII Zw 403, but derived such a low rotational velocity that we cannot positively state that a disk is a valid solution for this object.



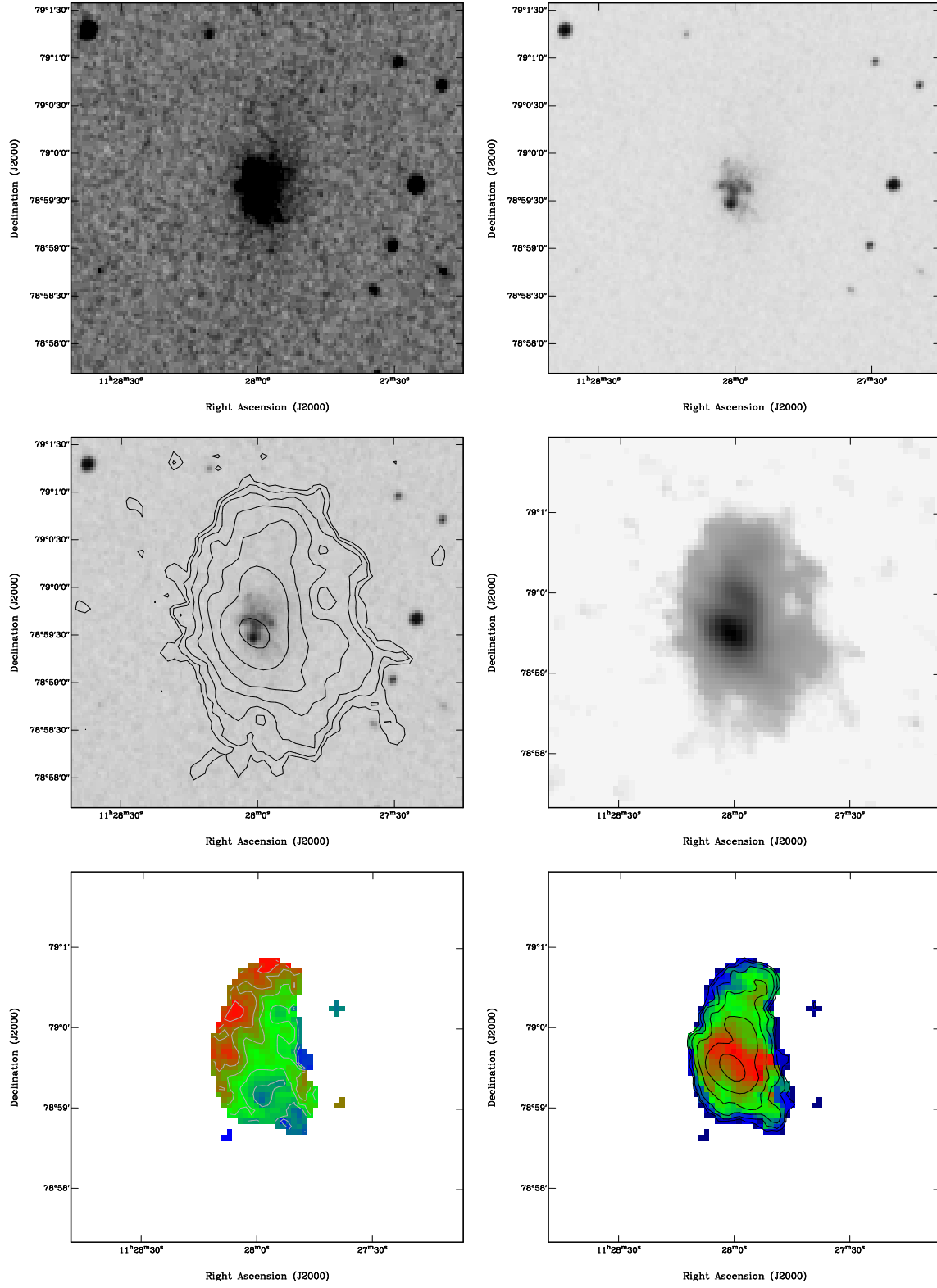


Figure 2.12: VII Zw 403. From left to right and top to bottom : DSS showing the extent of the galaxy; DSS showing the star-forming regions; DSS (greyscale) and Moment 0 (contours); Moment 0; Moment 1 (contours and pseudo colours); Moment 0 (contours) and Moment 2 (pseudo colours).

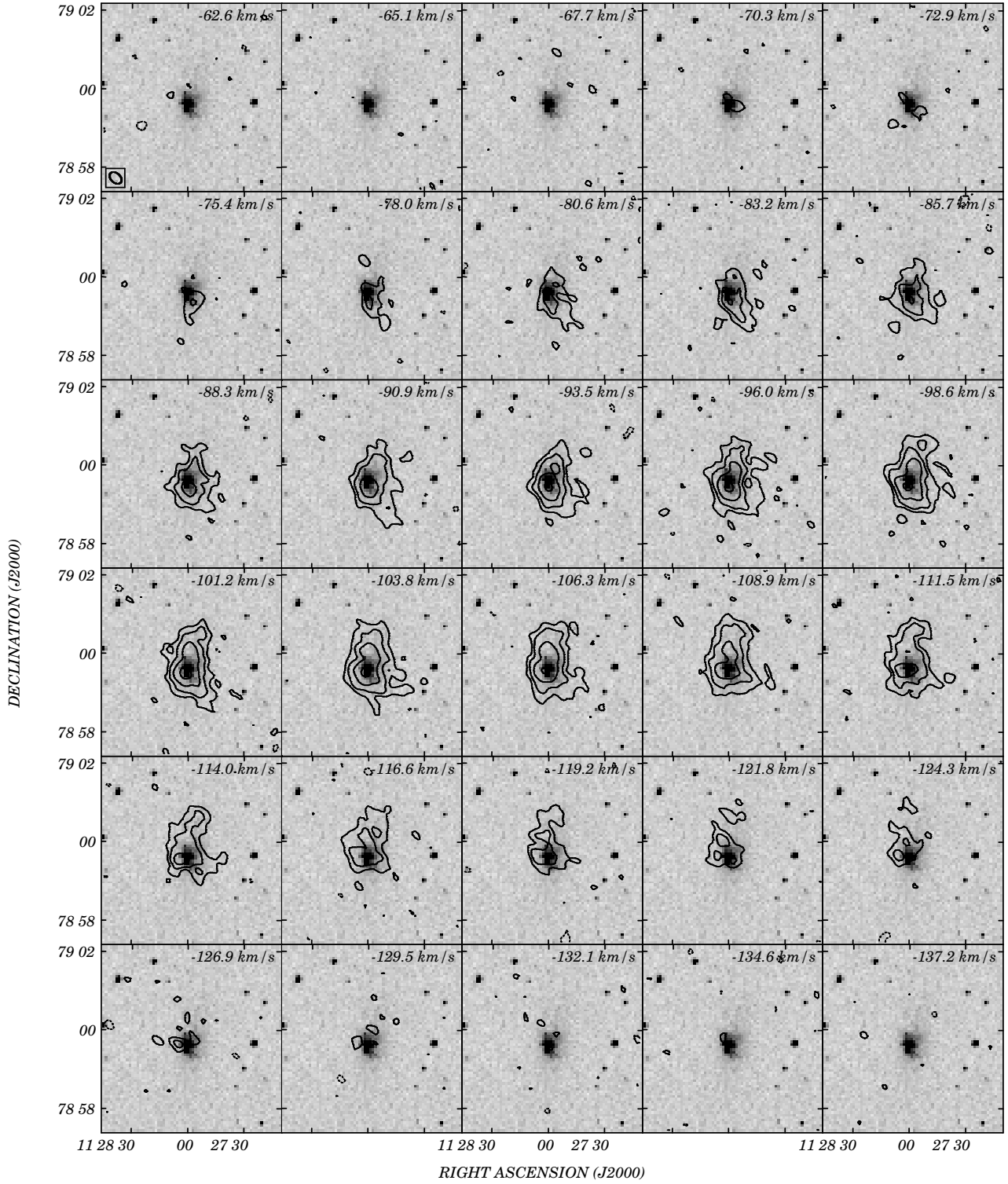


Figure 2.13: Channel maps for VII Zw 403. Contours are  $-3.60 \times 10^{19}$ ,  $3.60 \times 10^{19}$ ,  $7.20 \times 10^{19}$ ,  $1.44 \times 10^{20}$  and  $2.88 \times 10^{20}$  atoms per square centimeter.

$\alpha_0$	$\delta_0$	P.A. (deg)	$i$ (deg)	$V_0$ (km/s)	$V_m$ (km/s)	$R_m$ (arcsec)
11h28m04.40s	78d59m32.58s	227.05	52.71	-102.80	10.95	95.82

Table 2.7: Kinematical fit parameters for VII Zw 403

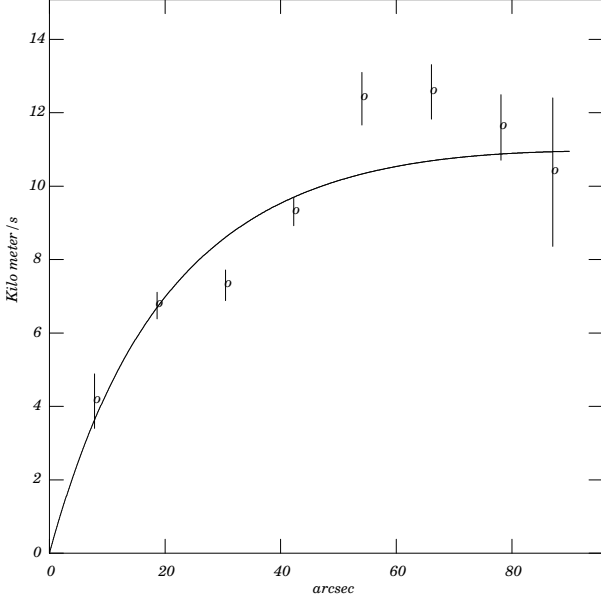


Figure 2.14: Rotation curve for VII Zw 403.

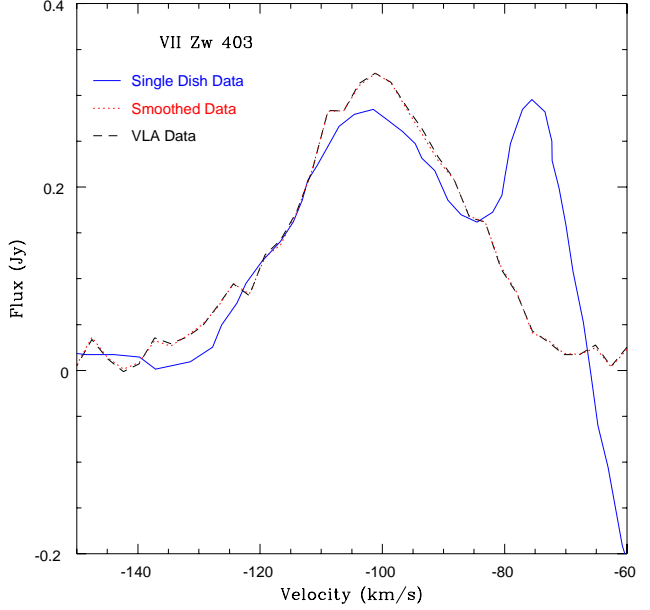


Figure 2.15: Spectra for VII Zw 403.

## 2.4.4 Velocity dispersion

A quick look at the velocity dispersion map shown in fig. 2.12 would have us say that we merely have the largest dispersion where the gas is at its densest. This is certainly true, but a closer look at the map shows that the high dispersion region is actually a thin stripe in between the two peaks that we noticed before. This supports the hypothesis that there are in fact two different clouds in the process of merging. The overlapping of kinematically different components would result in a greater velocity dispersion, which can also be due to the star forming knots. In effect, it reaches  $(\sigma)_{peak} = 12.7$  km/s in this region, while the mean is  $\sigma = 7.8$  km/s. We can also see now that we have  $V_m/\sigma \simeq 1$ .

## 2.5 Haro 2

### 2.5.1 Morphology

Haro 2 appeared to us as a quite boring object. We have a poor resolution, which is due to the distance to this galaxy, and the one thing we can say is that it has a single HI peak near the center of the total gas distribution. There is also a companion cloud to the north-east.

### 2.5.2 H I flux - comparison with single dish

The various measurements are as usual presented in a table, 2.8. We had quite a hard time determining these values because the low level of the emission makes it very difficult to distinguish between “real” emission and artifacts due to CLEANing or smoothing. The fluxes listed reflect what we believe. Note that our best value (3.4 Jy.km/s) represents 78 % of Thuan and Martin’s flux.

Flux determination (Jy.km/s)	Robust=1 data	Smoothed data
Zeroth moment	1.56	2.56
Aperture Photometry	3.0	3.3
Spectrum Integration	3.25	3.4

Table 2.8: Flux values for Haro 2

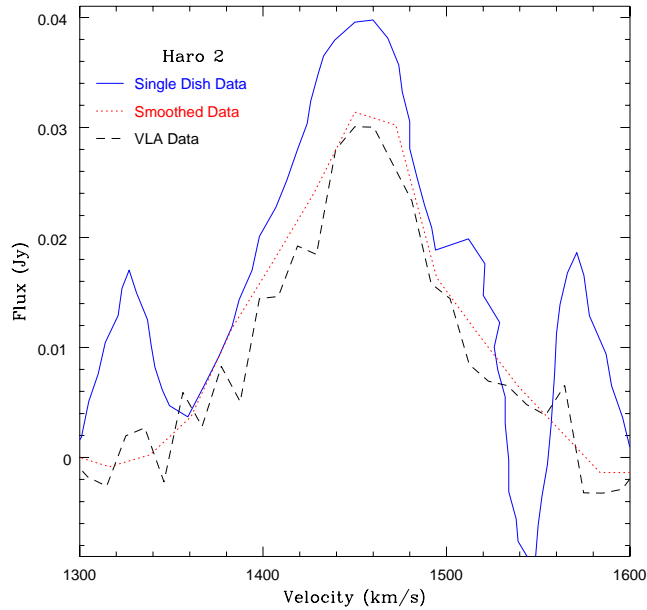


Figure 2.16: Spectra for Haro 2.

### 2.5.3 Kinematical modeling

There was absolutely no kinematical modeling for Haro 2. Our resolution was too poor to get a decent number of points on any rotation curve, and the algorithm we used (task GAL) proved highly unstable in that case. We therefore have no reliable rotational velocity for Haro 2.

### 2.5.4 Velocity dispersion

Again there is not much to say here. The mean velocity dispersion is  $\sigma = 16.1$  km/s which is significantly high, but with the resolution we have for Haro 2, this is to be taken with a bit of salt, because different parts of the galaxy, with different velocities, might be unresolved, thus resulting in a broader line.

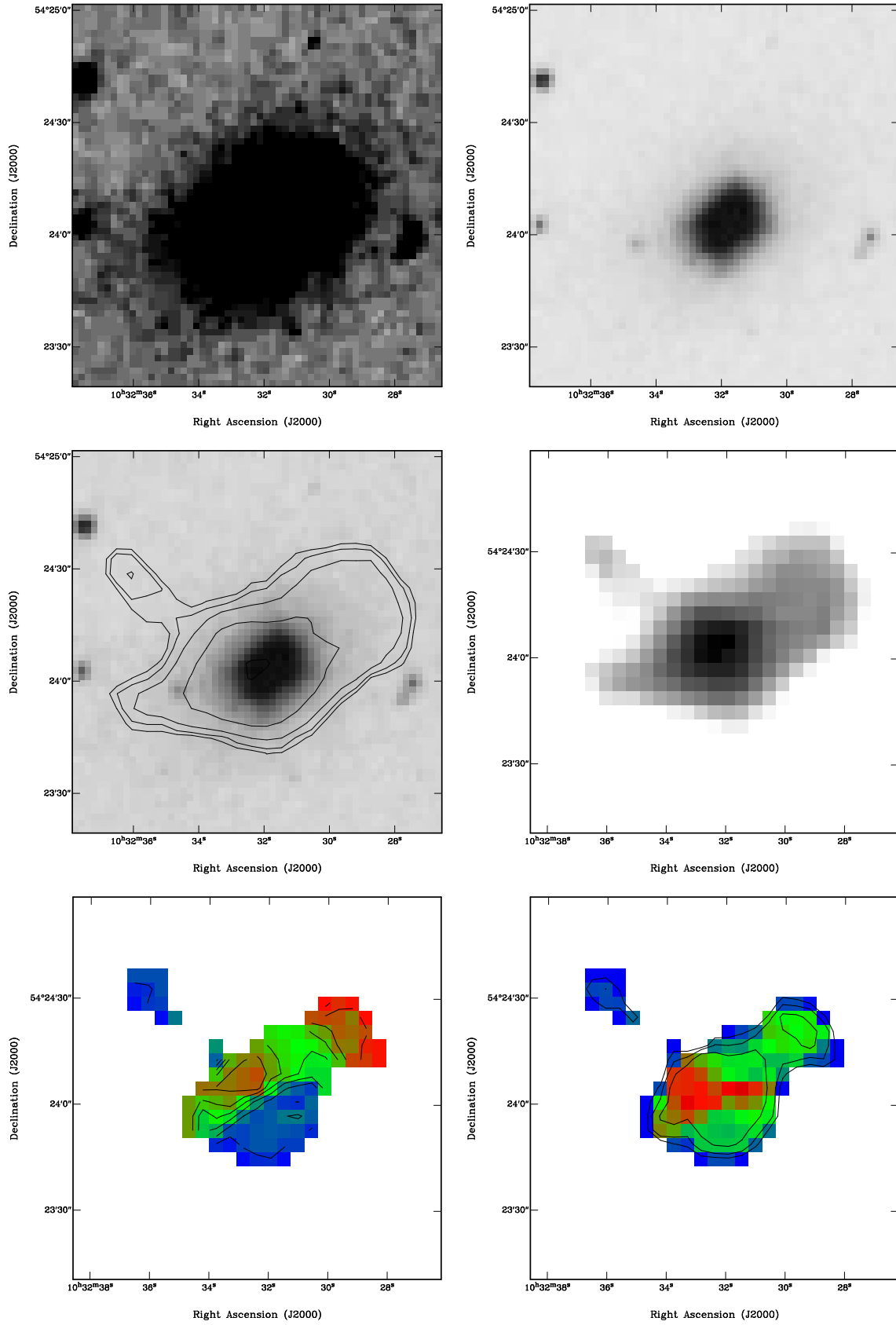


Figure 2.17: Haro 2. From left to right and top to bottom : DSS showing the extent of the galaxy; DSS showing the star-forming regions; DSS (greyscale) and Moment 0 (contours); Moment 0; Moment 1 (contours and pseudo colours); Moment 0 (contours) and Moment 2 (pseudo colours).

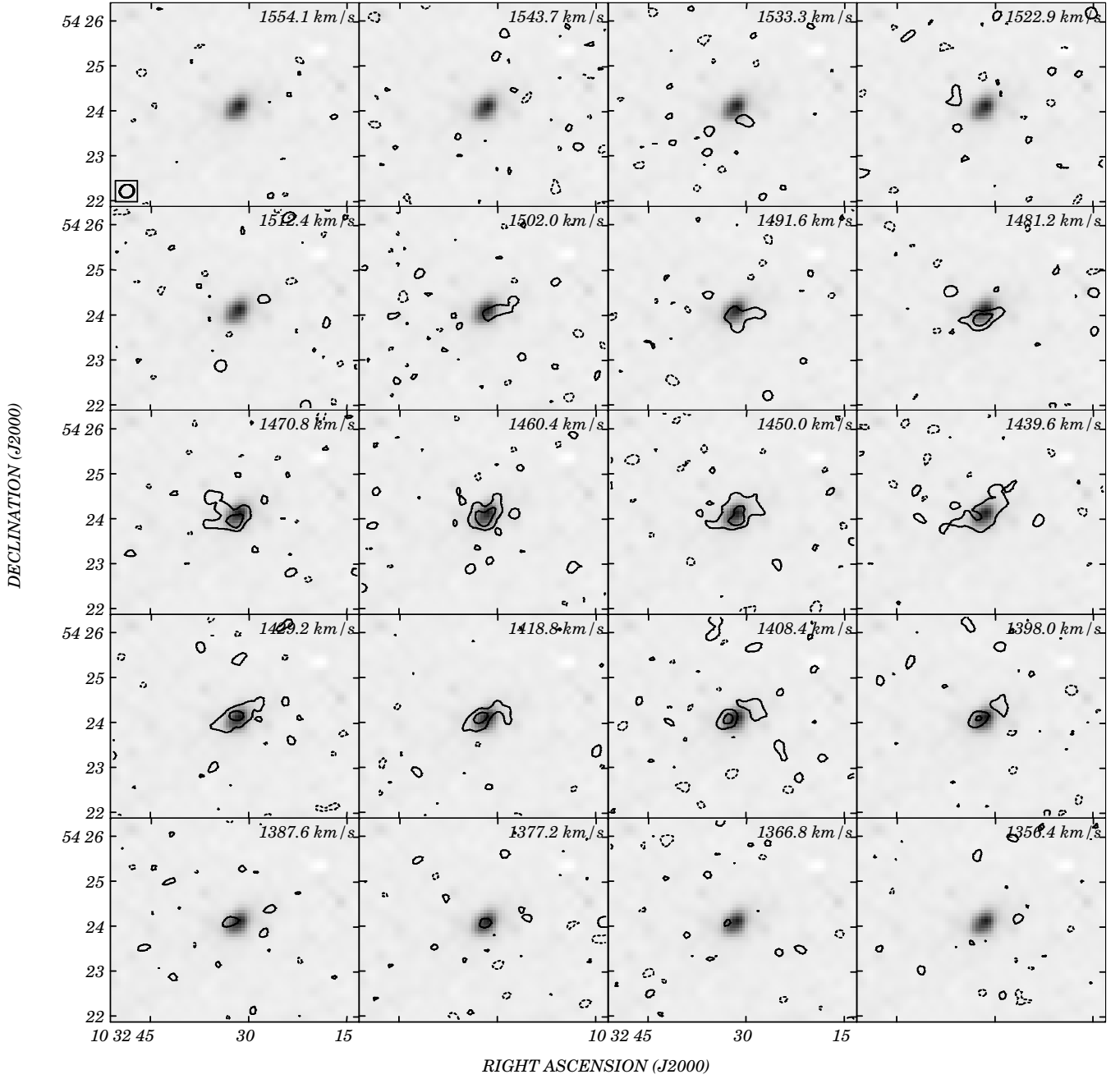


Figure 2.18: Channel maps for Haro 2. Contours are  $-7.25 \times 10^{19}$ ,  $7.25 \times 10^{19}$  and  $1.45 \times 10^{20}$  atoms per square centimeter.

## 2.6 The dark matter problem

### 2.6.1 A very brief overview

In the framework of Newton’s theory of gravitation, the rotational velocity of a galaxy should first rise in the inner regions, then turn over and decrease as  $r^{-1/2}$ . However, this is not what is observed. First with optical data and now with the more extended neutral hydrogen rotation curves, it appears that, in most galaxies, rotational velocities either do not decrease or that they do so very slowly. This suggests that there exists a large halo of *dark matter* surrounding these galaxies<sup>6</sup>. Dark matter does not seem to radiate and can only be detected through its gravitational influence. The form of this dark matter is unknown at the moment, but there are two major classes of objects that could account for it : MACHOs and WIMPs. MACHO stands for Massive Compact Halo Object and this term encompasses all sorts of large and dark baryonic objects that are supposed to exist within the halos of galaxies : rogue planets, black holes, brown dwarfs and the like. There have been experiments to detect the presence of such objects via gravitational microlensing (EROS in Europe and MACHO project in the USA). WIMP is an acronym for Weak Interacting Massive Particle and a prototype of such a particle is the neutrino. A team in Japan has recently established that this particle does have a mass, which could at least partly account for some of the dark matter.

### 2.6.2 Dark matter in our sample

#### Introduction

Our purpose here is to determine if there is dark matter in the objects we are studying, and if so, in what proportions. To this end, we will need to calculate their total masses  $M_T$ . From there, we can deduce the amount of dark matter  $M_{dark}$  via

$$M_{dark} = M_T - \frac{5}{4}M_H - M_{H_2} - \left(\frac{M_*}{L_B}\right) L_B. \quad (2.3)$$

The factor  $5/4$  is supposed to take into account the mass of helium in the interstellar medium and the mass-to-light ratio  $M_*/L_B$  is chosen according to the galaxy’s stellar population. We followed the empirical relation given in [20]:

$$\frac{M_*}{L_B} = 0.668 + 0.039(10 - T)^2 \quad (2.4)$$

where  $T$  is the morphological type index as given in [12]. For our sample of BCDs,  $T = 10$ , and therefore  $M_*/L_B = 0.668$ . The mass  $M_{H_2}$  of molecular hydrogen is quite difficult to determine, because this element has few ways to radiate, and is therefore almost “invisible”. Its presence is inferred with accompanying molecules, such as CO. Many observations have failed to detect dwarfs in the CO spectral line, and we will therefore assume  $M_{H_2}$  to be negligible.

#### Determination of $M_H$

The HI mass  $M_H$  is computed from the total flux  $S_H$  using equation (2.2). It is quite clear from the comparison of our fluxes with those in [44] that the VLA does not recover as much flux as single dish telescopes<sup>7</sup>. We will therefore use the latter to determine  $M_H$ . Now, single dish radioastronomers

---

<sup>6</sup>Some have even suggested to modify newtonian dynamics to solve this problem [29].

<sup>7</sup>The exception here seems to be I Zw 49.

perform a correction to their raw fluxes, in order to account for the source’s HI size with respect to that of the primary beam. The corrected flux is given by

$$S_c = S_H \sqrt{\left(1 + (a_{50}/\theta)^2\right) \left(1 + (b_{50}/\theta)^2\right)} \quad (2.5)$$

where  $\theta$  is the size of the telescope’s primary beam at half power point<sup>8</sup> and  $a_{50}$  and  $b_{50}$  are respectively the major and minor axis of the ellipse fitting the HI distribution at 50 % of the peak, and are only accessible through mapping observation. Single dish astronomers adopt average empirical values based on a galaxy’s optical size.

Since we have access to  $a_{50}$  and  $b_{50}$  from our maps, we chose to calculate the “true” corrections to single dish fluxes using those values. The results are given in table 2.9.

Parameter	NGC 2366	I Zw 49	VII Zw 403	Haro 2
$S_H$ (Jy.km/s)	202.6	31.8	14.3	4.4
$a_{50}$ (″)	92.8	224	77.2	73.6
$b_{50}$ (″)	65.5	61	51.6	29.3
$S_c$ (Jy.km/s)	205.7	33.8	14.4	4.4
$D$ (Mpc)	3.54	7.2	4.5	20.5
$M_H$ ( $10^8 M_\odot$ )	6.08	4.13	0.69	4.40

Table 2.9: Corrected fluxes and HI masses.

## Determination of $M_T$

We found the calculation of the total mass to be in some debate. Most authors use a simple dynamical mass following the equation

$$M_T = G^{-1} r_H V_{rot}^2 \quad (2.6)$$

where  $r_H$  is the radius of the HI distribution and  $V_{rot}$  the rotational velocity at this point. This is fine as long as the HI lies in a disk, but for dwarfs, this might not be a good approximation. To find a dynamical equation for these systems, we referred to the study of nine dwarf irregulars by Lo, Sargent and Young [26]. Their application of the virial theorem leads to the following equation :

$$M_T = G^{-1} \beta r_H \alpha \sigma_v^2 [1 + (V_{rot}/\sigma_{3D})^2], \quad (2.7)$$

where  $\sigma_v$  is the radial velocity dispersion, which is supposed to be related to the three-dimensional dispersion  $\sigma_{3D}$  through  $\sigma_{3D}^2 = \alpha \sigma_v^2$  with  $\alpha = 3$  in the isotropic case.  $\beta$  is a parameter that describes the shape of the rotation curve, and they adopt  $\beta = 1.35$ .  $r_H$  is now the HI radius taken at 10 % of the peak. The last factor represents the cloud motions which arise only from gravitational forces. Lo *et al.* assume that this is the total line width,  $\sigma_T$ , minus the broadening due to non gravitational forces,  $\sigma_{turb}$ , i.e.,

$$\sigma_v^2 [1 + (V_{rot}/\sigma_{3D})^2] \simeq \sigma_T^2 - \sigma_{turb}^2 \equiv \sigma_{c-c}^2. \quad (2.8)$$

They adopt  $\sigma_T = \Delta V_{50}/2.36$  and  $\sigma_{turb} = \sigma_{HI}$ , where  $\sigma_{HI}$  is the average velocity dispersion measured in the moment 2 maps. This last equation is obviously correct when HI dispersion is entirely due to non-gravitational forces, such as the effects of star formation, gas viscosity or magnetic fields. However, when  $\sigma_{c-c} < \sigma_{HI}$ , this leads to the situation that the gas motions are too large for the HI

<sup>8</sup> $\theta = 10.8'$  for the NRAO’s 300-foot telescope.



to remain bound to the galaxy, and the gas would disperse, which is unlikely. We therefore decided to bound  $M_T$  by two limiting assumptions, a lower limit assuming, as Lo *et al.*, that HI dispersion is due to non-gravitational effects

$$M_T^{low} = 9.3 \times 10^5 r_H \sigma_{c-c}^2, \quad (2.9)$$

and an upper limit assuming that dispersion is entirely due to gravity,  $\sigma_{turb} = 0$

$$M_T^{up} = 9.3 \times 10^5 r_H \sigma_T^2. \quad (2.10)$$

## dIs and BCDs

One of our concerns in this work was precisely to compare BCDs and dIs. Lo *et al.*'s sample provides us a good opportunity to do so<sup>9</sup>. We follow their method, amended as described in the previous section. The results are summarized in table 2.10 and plotted in fig. 2.19. There are a few things we can comment on. First, it appears quite clearly that the faintest objects tend to have higher  $M_T/L_B$  ratios than BCDs. This suggests the existence of a threshold, seen both in luminosity ( $M_B \simeq 13$ ) and total mass ( $M_T \simeq 10^8 M_\odot$ ), below which galaxies have a lesser star formation efficiency (having formed fewer stars per unit mass) and above which they attain a maximum efficiency that remains constant with mass and luminosity. This trend has already been noticed by Freeman [18]. Secondly, the dark matter and gas contents of these objects do not seem to exhibit clear relationships with luminosity or total mass. The one thing we can say is that faint and low-mass objects appear to be very dark matter dominated ( $M_{dark}/M_T > 70\%$ ), but further studies with a larger, statistically more meaningful sample will definitely be needed to confirm this. Lastly, and this is best seen in table 2.10, our objects appear to have a somewhat higher velocity dispersion  $\sigma_{HI}$  than Lo *et al.*'s dIs, which is not quite surprising since they are currently undergoing violent episodes of star formation, and therefore have a more disturbed interstellar medium.

Source	$\Delta V_{50}$ (km/s)	$\sigma_T$ (km/s)	$\sigma_{HI}$ (km/s)	$\sigma_{c-c}$ (km/s)	$r_H$ (kpc)	$M_T^{low}$ ( $10^7 M_\odot$ )	$M_T^{up}$ ( $10^7 M_\odot$ )	$M_H$ ( $10^7 M_\odot$ )	$L_B$ ( $10^6 L_\odot$ )
LGS-3	17.5	7.5	4.0	6.5	0.45	1.8	2.4	0.02	0.7
UGC 4483	30.5	13.0	6.5	11.0	1.0	11.2	15.7	3.7	23.0
DDO 69	19.0	8.0	5.0	6.0	1.1	3.7	6.6	3.6	36.0
CVn dwA	22.5	9.5	6.0	7.5	1.5	7.8	12.6	8.1	11.0
DDO 155	25.0	10.5	6.0	9.0	0.4	3.0	4.1	0.2	2.3
DDO 187	30.5	13.0	8.5	9.8	1.1	9.8	17.3	5.0	23.0
Sag DIG	19.0	8.0	4.0	7.0	0.84	3.8	5.0	0.8	2.5
DDO 210	18.5	8.0	4.5	6.6	0.35	1.4	2.1	0.3	1.3
DDO 216	24.0	10.0	4.5	9.0	0.83	6.2	7.7	1.3	69.0
NGC 2366	109.6	46.4	7.7	45.8	2.67	521	535	60.8	810
I Zw 49	80.0	33.9	8.4	32.8	3.05	306	326	41.3	1090
VII Zw 403	34.1	14.4	7.8	12.2	1.05	14.4	20.4	6.9	72
Haro 2	90.4	38.3	16.1	34.8	2.92	328	398	44.0	2910

Table 2.10: Comparison of our BCDs and Lo *et al.*'s dIs

<sup>9</sup>We will probably use a much larger sample (70 dIs) studied by Hoffman *et al.* [20] in a future article.

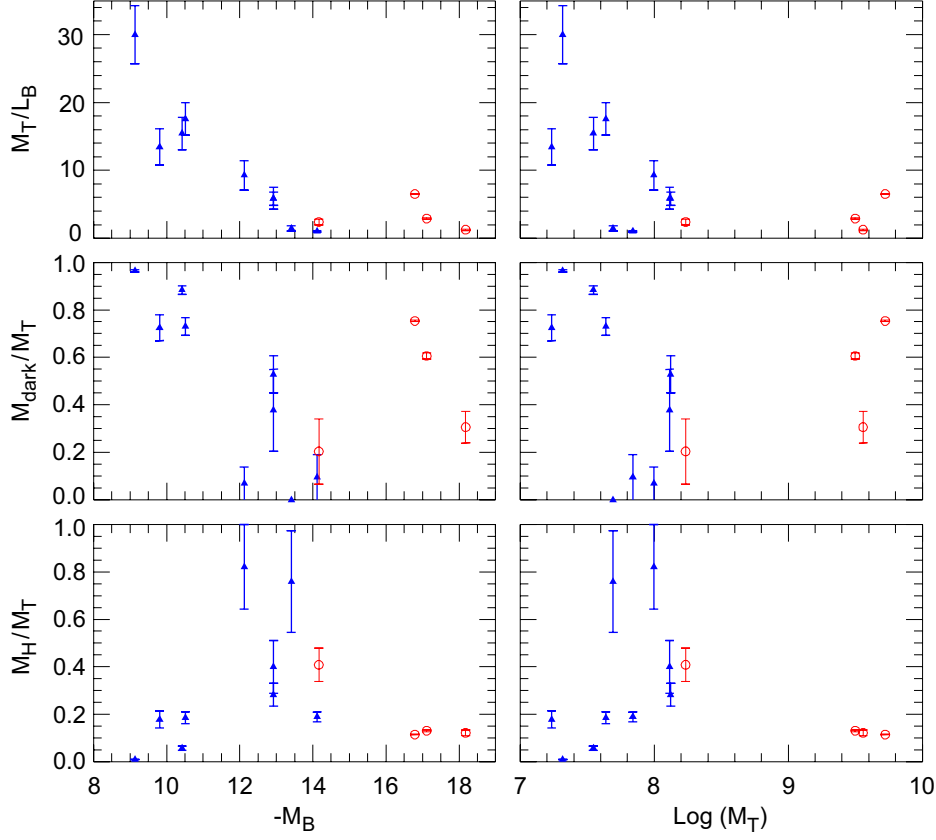


Figure 2.19: Comparison of our BCDs (in red) and Lo *et al.*'s dIs (in blue).

## Conclusions

We have presented VLA data on four Blue Compact Dwarfs from the Thuan & Martin sample [44]. We have mapped their HI contents, derived their total fluxes and studied their kinematics. It is to be noted that there are not many such studies as of yet.

The interstellar medium in these objects shows evidence of great disturbances, with holes and clumps in the HI distribution, which are especially visible in NGC 2366 and I Zw 49. These two objects appeared in the kinematical modelling to be rotationally dominated, whereas random motions in VII Zw 403 and Haro 2 seem to be at least as important as rotational motions.

We have also detected HI cloud companions around I Zw 49 and Haro 2.

While finally addressing the dark matter problem, we have presented a comparison between our sample and the nine dwarf irregulars studied by Lo, Young & Sargent [26]. The only difference between BCDs and dIs we can derive from this quick comparison, apart from the fact that our objects are more massive, seems to be a better star formation efficiency in BCDs, which results in a higher velocity dispersion. Both types of objects seem to be otherwise quite similar. Whether there is an evolutionary path, such as merging, from one type to the other is another question altogether.

# Bibliography

- [1] Andrews, H.C., & Hunt, B.R. *Digital Image Restoration*, Prentice-Hall, 1977
- [2] Aparicio, A. *et al.*, AJ, **110**, 212, 1995
- [3] Binney, J., & De Vaucouleurs, G. MNRAS, **194**, 679, 1981
- [4] Bosma, A., Van Der Hulst, J.M., & Athanassoula, E. A&A, **198**, 100, 1988
- [5] Briggs, D.S. *High-fidelity deconvolution of moderately resolved sources*, PhD. Thesis, 1995
- [6] Clark, B.G. A&A, **89**, 377, 1980
- [7] Clark, B.G. in *Synthesis Imaging In Radio Astronomy*, A.S.P.C.S., **6**, 1989
- [8] Comins, N.F., ApJ, **266**, 543, 1983
- [9] Comins, N.F. ApJ, **284**, 90, 1984
- [10] Cornwell, T.J., & Evans, K.F. A&A, **143**, 77, 1985
- [11] Cornwell, T.J., & Braun, R. in *Synthesis Imaging In Radio Astronomy*, A.S.P.C.S., **6**, 1989
- [12] de Vaucouleurs G., de Vaucouleurs, A., Corwin, H.G., Buta, R.J., Paturel, G., & Fouque, P. *Third Reference Catalog of Bright Galaxies*, Springer-Verlag, 1991
- [13] Dickel, J.R., & Rood, H.J. ApJ, **223**, 391, 1978
- [14] Efstathiou, G., & Silk, J. FoCP, **9**, 1, 1983
- [15] Fanelli, M.N., O'Connell, R.W., & Thuan, T.X. ApJ, **334**, 665, 1988
- [16] Fisher, J.R., & Tully, R.B. ApJS, **47**, 139, 1981
- [17] Fomalont, E.B., & Perley, R.A. in *Synthesis Imaging In Radio Astronomy*, A.S.P.C.S., **6**, 1989
- [18] Freeman, K.C., in *Nearly Normal Galaxies*, Springer-Verlag, 1987
- [19] Gerola, H., Seiden, P.E., & Schulman, L.S. ApJ, **242**, 517, 1980
- [20] Hoffman, G.L., Salpeter, E.E., Farhat, B., Roos, T., Williams, H., & Helou, G. ApJS, **105**, 269, 1996
- [21] Högbom, J. ApJS, **15**, 417, 1974
- [22] Hunter, D.A. ApJ, **260**, 81, 1982
- [23] Kennicutt, R.C., Balick, B., & Heckman, T. PASP, **92**, 134, 1980

- [24] Kennicutt, R.C., Jr., Edgar, B.K., & Hodge, P.W. ApJ, **337**, 761, 1989
- [25] Kennicutt, R.C., Jr. ApJ, **287**, 116, 1984
- [26] Lo, K.Y., Sargent, W.L.W., & Young, K. AJ, **106**, 507, 1993
- [27] Loose, H.H., & Thuan, T.X. in *Star-forming Dwarf Galaxies*, Frontières, 1986
- [28] Loose, H.H., & Thuan, T.X. ApJ, **309**, 59, 1986
- [29] Milgrom, M. ApJ, **270**, 365, 1983
- [30] Napier, P.J., Thompson, A.R., & Ekers, R.D. IEEEP, **71**, 1295, 1983
- [31] Pantin, E., & Starck, J.-L. A&AS, **118**, 575, 1996
- [32] Roelfsema, P. in *Synthesis Imaging In Radio Astronomy*, A.S.P.C.S., **6**, 1989
- [33] Roy, J.-R., Boulesteix, J., & Grundseth, B. ApJ, **367**, 141, 1991
- [34] Sargent, W.L.W., & Searle, L. ApJ, **162**, 155, 1970
- [35] Schulte-Ladbeck, R.E., Crone, M.M., & Hopp, U. ApJL, **493**, 23, 1998
- [36] Schwab, F.R. AJ, **89**, 1076, 1984
- [37] Searle, L., & Sargent, W.L.W. ApJ, **173**, 25, 1972
- [38] Skillman, E.D., & Kennicutt, R.C., Jr. ApJ, **411**, 655, 1993
- [39] Sramek, R.A., & Schwab, F.R. in *Synthesis Imaging In Radio Astronomy*, A.S.P.C.S., **6**, 1989
- [40] Staveley-Smith, L., Davies, R.D., & Kinman, T. MNRAS, **258**, 334, 1992
- [41] Taylor, C.L. ApJ, **480**, 524, 1997
- [42] Thompson, A.R., in *Synthesis Imaging In Radio Astronomy*, A.S.P.C.S., **6**, 1989
- [43] Thuan, T.X., & Seitzer, P.O. ApJ, **231**, 680, 1979
- [44] Thuan, T.X., & Martin, G.E. ApJ, **247**, 823, 1981
- [45] Thuan, T.X. ApJ, **268**, 667, 1983
- [46] Thuan, T.X. ApJ, **299**, 881, 1985
- [47] Thuan, T.X. in *Massive Stars in Starbursts*, Cambridge University Press, 1991
- [48] Thuan, T.X., & Izotov, Y.I. ApJ, **489**, 623, 1997
- [49] Viallefond, F., & Thuan, T.X. ApJ, **269**, 444, 1983
- [50] Van Der Hulst, J.M., Skillman, E.D., Smith, T.R., Bothun, G.D., McGaugh, S.S., & De Blok, W.J.G. AJ, **106**, 548, 1993
- [51] Wevers, B.M.H.R., Van Der Kruit, P.C., & Allen, R.J. A&AS, **66**, 502, 1986